MASTERARBEIT / MASTER'S THESIS

Titel der Masterarbeit / Title of the Master's Thesis

„Nitrogen Doping of Free-Standing Monolayer Graphene by Low-Energy Plasma Treatment“

verfasst von / submitted by

Tobias Görlich, BSc

angestrebter akademischer Grad / in partial fulfillment of the requirements for the degree of

Master of Science (MSc)

Wien, 2018 / Vienna, 2018

Studienkennzahl lt. Studienblatt / degree programme code as it appears on the student record sheet:	A 066 876
Studienrichtung lt. Studienblatt / degree programme as it appears on the student record sheet:	Physik / Physics
Betreut von / Supervisor:	Univ.-Prof. Dipl.-Phys. Dr. Jannik C. Meyer

Abstract

Reliable and efficient production of n-type graphene is crucial to further development of graphene-based electronic devices, such as transistors. A promising approach for the tuning of band gap and carrier concentration in graphene is nitrogen doping via post-synthesis plasma treatment. Low-energy ion irradiation is used to implant nitrogen atoms into suspended single-layer graphene. Pyrrolic, graphitic and pyridinic doping sites are observed and atomic resolution STEM images are presented. Single-atom EELS is utilized for a definite identification of nitrogen atoms and a series of spectrum images is created. A doping concentration of about 2 at.% is reached with an ion dose equivalent to 7 at.%. With 49 %, about half of nitrogen structures is pyrrolic, 42 % appear to be graphitic and 9 % pyridinic. Graphitic nitrogen is observed in three different configurations. Those are structures with the nitrogen atom being part of three hexagons (6-6-6), two hexagons and a heptagon (6-6-7) and two hexagons and an octagon (6-6-8). Regarding pyrrolic nitrogen, only three-bond structures are found. Only considering penta-, hexa- and heptagons, five of six possible three-bond structures are observed, namely 5-5-6, 5-5-7, 5-6-6, 5-6-7 and 5-7-7. A doping site consisting of three pentagons (5-5-5) is not observed. Generally, it is found that pyrrolic nitrogen sites that, in the introduced nomenclature, have more hexagons and have a cross sum closer to 18 are more common than others. Pyridinic sites that include a single vacancy and one (1N+SV), two (2N+SV) and three (3N+SV) nitrogen atoms are observed. Under the electron beam, transformations from all three kinds of implanted nitrogen into others are observed. However, no transformation from 6-6-6 graphitic nitrogen into another is observed, although they are detected frequently. The most severe challenges are the low reproducibility of results and contamination as an effect of the plasma treatment.

Kurzfassung

Für die weitere Entwicklung von auf Graphen basierter Elektronik, z.B. Transistoren, ist es essentiell, n-dotiertes Graphen verlässlich und effizient erzeugen zu können. Stickstoffdotierung durch Plasmabestrahlung nach der Herstellung des Graphens ist ein vielversprechender Ansatz zur gezielten Beeinflussung von Bandlücke und Ladungsträgerkonzentration. Um Stickstoffatome in das Graphengitter zu implantieren, wird frei stehendes einlagiges Graphen mit Ionen niedriger Energie bestrahlt. Atomar aufgelöste STEM Bilder von pyrrolischen, graphitischen und pyridinischen Stickstoffdefekten werden gezeigt. Zur eindeutigen Identifizierung von Stickstoffatomen wird atomare EELS verwendet. Zudem werden mehrere Spectrum Images erzeugt. Eine Stickstoffkonzentration von rund 2 at.% wird mit einer Ionendosis, die 7 at.% enstspricht, erreicht. Mit 49% ist ungefähr die Hälfte der erzeugten Stickstoffstrukturen pyrrolisch, während 42% graphitisch sind und 9% pyridinisch. Graphitischer Stickstoff wird in drei verschiedenen Konfigurationen beobachtet. In einer ist das Stickstoffatom Teil von drei Hexagonen (6-6-6), in der zweiten von zwei Hexagonen und einem Siebeneck (6-6-7) und in der dritten von zwei Hexagonen und einem achtatomigen Ring (6-6-8). Pyrrolischer Stickstoff wird ausschließlich mit drei Bindungen beobachtet. Wenn nur Fünf-, Sechs- und Siebenecke berücksichtigt werden, dann sind sechs verschiedene solcher pyrrolischer Verbindungen möglich. Fünf davon werden beobachtet, nämlich 5-5-6, 5-5-7, 5-6-6, 5-6-7 und 5-7-7, pyrrolischer Stickstoff mit drei Fünfecken (5-5-5) nicht. Pyrrolischer Stickstoff wird im Allgemeinen dann häufiger verzeichnet, wenn in der eingeführten Nomenklatur erstens mehr Hexagons angeführt sind und zweitens die Quersumme näher an 18 liegt. Pyridinischer Stickstoff wird in Konfigurationen beobachtet, die eine Leerstelle und ein (1N+SV), zwei (2N+SV) und drei (3N+SV) Stickstoffatome umfassen. Transformationen von allen drei Dotierungsarten in andere werden unter dem Elektronenstrahl beobachtet. Obwohl 6-6-6 graphitischer Stickstoff vielfach beobachtet wird, wird keine Transformation dieser Struktur in eine andere aufgezeichnet. Die größten Herausforderungen sind die geringe Vergleichbarkeit der Ergebnisse und die Kontamination, die eine Folge der Plasmabestrahlung ist.

Contents

Abstract **III**

Kurzfassung **V**

1 Introduction **1**

1.1 Graphene 1

1.2 Nitrogen Doping of Graphene 2

1.3 Electron Microscopy 4

2 Transmission Electron Microscopy **5**

2.1 Electron Sources 5

2.2 Electron Optics 6

2.3 Electron-Sample Interaction 9

2.4 Electron Detectors - STEM and EELS 10

3 State of the Art **13**

3.1 Simulation 13

3.2 Experimental 16

3.3 Aims and Approach 20

4 Experimental Setup **23**

4.1 Sample Preparation 23

4.2 Analysis 32

5 Results and Discussion **35**

5.1 Overview 35

5.2 Nitrogen Configurations 37

5.2.1 Pyrrolic 37

5.2.2 Pyridinic 39

5.2.3 Graphitic 41

5.2.4 Distribution of Nitrogen Species 44

5.3 Large Field-of-View Spectrum Image 48

6 Conclusion and Outlook **51**
6.1 Conclusion 51
6.2 Outlook 52

Appendix **55**

List of Abbreviations **69**

List of Nomenclature **72**

List of Figures **73**

List of Tables **75**

Bibliography **77**

Chapter 1

Introduction

1.1 Graphene

Graphene is the name given to isolated layers of graphite. Prior to its first synthesis it has been considered unstable at finite temperatures, just as two-dimensional materials in general [1]. However, in 2004, K. S. Novoselov, A. K. Geim and co-workers were able to produce single graphene layers referred to as single-layer graphene (SLG) by mechanical exfoliation [2]. Besides graphene, other low-dimensional only-carbon solids are fullerenes in 0D and carbon nanotubes in 1D, while 3D only-carbon crystals are diamond and graphite [3]. Figure 1.1 shows these, excluding diamond.

Graphene consists of a honeycomb structure out of hexagons that can be thought of as benzene rings that lost their hydrogen atoms [5]. It exhibits weak Van der Waals-like out-of-plane interaction, but strong inplane sp^2 bonds [6]. Therefore, graphene shows a high mechanical stiffness. It is the strongest material ever measured [7]. Besides its unique mechanical properties, graphene features a high thermal conductivity of about $5000\,\mathrm{W\,mK^{-1}}$ and carrier mobility of up to $\approx 200{,}000\,\mathrm{cm^2\,V^{-1}\,s^{-1}}$ [8]. For a detailed explanation of the electronic properties of graphene, see [5]. An introduction to the band structure of graphene can be found in section 1.2.

Mechanical exfoliation was the first successful approach to produce graphene. However, since then other ways of synthesizing graphene have been realized successfully, most prominently chemical vapor deposition (CVD). Commonly, transition metals are used as substrate in CVD because of their carbon solubility when exposed to a hydrocarbon gas at high temperatures. Cooling the hot substrate leads to a decrease in solubility that leads to the nucleation of a thin carbon film. This allows the growth of large areas of high-quality SLG. Often used for CVD-synthesis of SLG are copper and methane. Other methods include chemical derivation from graphite oxide and total organic synthesis [1, 9].

The discovery of graphene has attracted great research interests in the fields of electrochemistry [1], photonics [10], thermology [11] and others. However, early on research efforts were focused on the field of nanoelectronics [2]. This is due to the unique electronic properties that graphene features [3, 5], some of which are mentioned in section

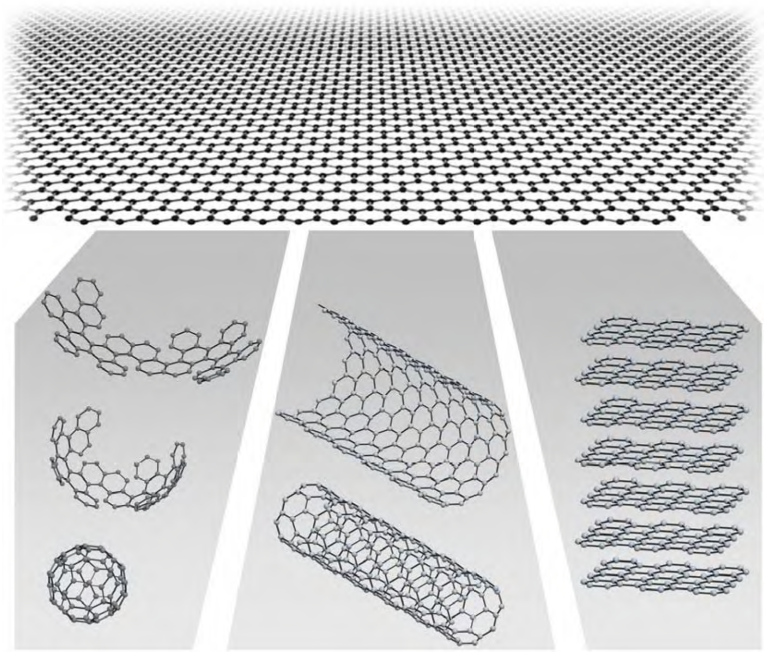

Figure 1.1: Structures related to graphene (top). Fullerene (bottom left), carbon nanotube (bottom center) and graphite (bottom right). It is illustrated how graphene could be wrapped up into fullerenes, rolled into nanotubes and stacked into graphite [4].

1.2. Since it had been believed that 2D materials were unstable in general, the successful synthesis of graphene has also lead to interest in many other 2D materials, such as hexagonal boron nitride (hBN) and molybdenum disulfide (MoS2).
The experiments in this thesis will be conducted with CVD-synthesized SLG.

1.2 Nitrogen Doping of Graphene

Nearest-neighbor tight-binding approximation leads to an electronic band structure of pristine graphene that is shown in Figure 1.2. As can be seen, pristine graphene features two band crossing points K and K' in its first Brillouin-zone, called Dirac points. The electron energy at the Dirac points depends linearly on the wave vector, similar to the Dirac spectrum of massless Fermions. The propagation of electrons in pristine graphene can, therefore, be described as the movement of charged massless particles. Graphene has thereby lead to the possibility of observing relativistic quantum particles [3].
Figure 1.2 shows that pristine graphene has no band gap. Valence and conduction band touch each other at the Dirac points. Around them, the density of states is small, but not 0. For this reason, it is possible to produce field-effect transistors (FET) using pristine graphene as shown in [2], but they suffer from low on-off ratios of approximately 30 for $T = 300K$. In order to achieve real off-states and an enhanced performance, besides confining graphene to nanoribbons [12] and introducing defects [13], graphene can be

doped with nitrogen to introduce a band gap [14]. It also grants the opportunity to significantly increase and fine tune the charge carrier density, which allows the definition of the electric current through semiconductor devices and enhanced on-states as well. This would enable graphene to be used in the production of high-speed electronics [1]. Graphene nanoelectronics is predicted to have the potential of introducing a post-silicon era [15], at least regarding high-performance applications.

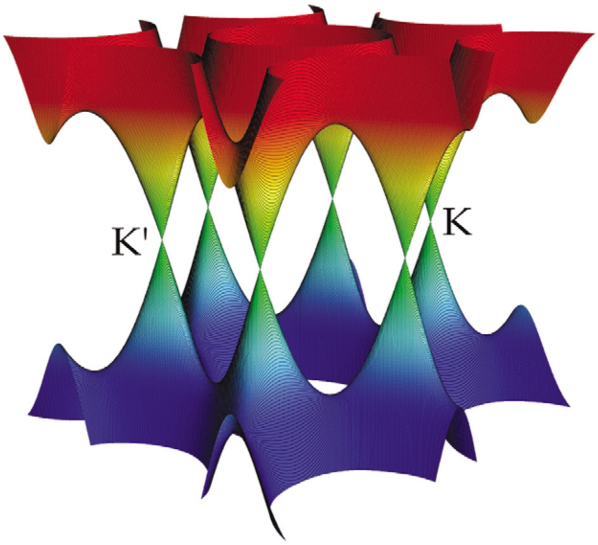

Figure 1.2: Band structure of pristine Graphene based on nearest-neighbor tight-binding approximation [3]

N-doped graphene is anticipated to have a large potential for future applications, while some have already been implemented in lab scale [16–22]. As mentioned, when graphene was firstly synthesized in [2], one application of pristine graphene was proposed and tested. A graphene-based FET [16] was expected to be smaller, consume less energy and operate at higher frequencies than traditional silicon-based semiconducting devices. At the cost of decreased mobility and conductivity, nitrogen-doped graphene offers the possibility of greatly enhanced off-states in comparison to pristine graphene. N-doped graphene can be utilized along with boron-doped graphene in p-n-junctions. Another potential industrial scale application of N-doped graphene are lithium ion batteries [16–18], in which it may serve as anode material. The high surface area, mechanical flexibility and electronic properties make graphene a favorable material. It was found that N-doped graphene may have almost twice the reversible discharge capacity of pristine graphene [17]. It is expected that the utilization of N-doped-graphene-based devices will allow high reversible capacities along with high charge and discharge rates. N-doped graphene may also be used in fuel cells [16, 19, 20] as electrocatalyst or simply as the catalysts support, in ultracapacitors [21] and electrochemical biosensors [22].

In this thesis, nitrogen doping will be implemented by plasma treatment. Advantages of and information about plasma treatments can be found in section 3.2.

1.3 Electron Microscopy

Abbe's resolution limit for aberration-corrected large-aperture lens light-optical compound microscopes predicts a best-possible object resolution limit of 0.3 µm for the middle of the visible electromagnetic spectrum. This allows the direct observation of biological objects, like cells [23]. However, if atomic structures, such as graphene, should be observed, this is not sufficient, as the distance between two atoms in graphene is $1.42\,\text{Å} = 0.142\,\text{nm}$ [5].

As it has been found in the early 20th century that particles like electrons possess wave-like character, it became thinkable to utilize electrons instead of light in microscopes. For an acceleration potential of 50 kV, the resolution limit is about 0.005 nm, which would be sufficient for the observation of atoms [23].

The setup of a transmission electron microscope (TEM) in principle equals that of a transmission light microscope. However, since the imaging particles are electrons instead of photons, firstly an electron source, secondly electron optics and thirdly an electron detector are needed. As it turns out, the resolution limit for electron microscopes is not given by Abbe's resolution limit any further. The resolution is limited by aberrations of the electron lenses. For achieving atomic resolution images of graphene, an aberration-corrected electron microscope is needed. In the experiment presented in this thesis, an aberration-corrected scanning transmission electron microscope (STEM) will be employed. This allows direct imaging of the atomic lattice of graphene samples prepared in the experiment. Electron energy loss spectroscopy (EELS) will be used as a support for the elemental identification. Further explanations on STEM and EELS can be found in chapter 2.

Chapter 2

Transmission Electron Microscopy

2.1 Electron Sources

One of the most essential parts of any TEM is a reliable source of electrons, also called electron gun. Generally, there are three kinds of electron guns. Firstly, there are thermionic sources, which rely on the emission of electrons from a hot cathode. Secondly, a strong local electric field can extract electrons from a material. Sources based on this effect are called field-emission guns (FEGs). Thirdly, a source based on both effects is called Schottky emitter. As cold FEGs offer many advantages, including a low energy spread, high current densities, no temperature perturbations and small probe sizes, they are utilized in the best performing TEMs and are most suitable for STEM and EELS application. Hence the focus of this section is on them.

To extract electrons from a material, the work-function barrier must be overcome. Therefor an electric field must be strong locally, which can be achieved by applying it to a sharp tip. The electric field lowers the work-function barrier of the material, commonly used is tungsten, and thereby allows electrons to tunnel out of it. The surface of the tip has to be pristine. This can be achieved by operating the TEM under UHV conditions ($<10^{-9}$ mbar).

Several parameters in a TEM are directly defined by the electron gun, such as its brightness. Brightness is the electron current per unit area and unit solid angle. It determines, for an electron beam of certain size, the amount of information that can be generated from a specimen in a certain time. Therefore, it plays a central role for small convergent probes, e.g. in STEM. A high brightness allows imaging of specimens with short exposure times, which minimizes instability effects, like sample drift. Related to the brightness is the electron source size. A smaller source allows higher brightness, but also enhances spatial coherency, which, for example, influences the quality of phase-contrast images and the sharpness of diffraction patterns. Most importantly though, the sharpness of the tip defines a resolution limit for the microscope. On the contrary, small

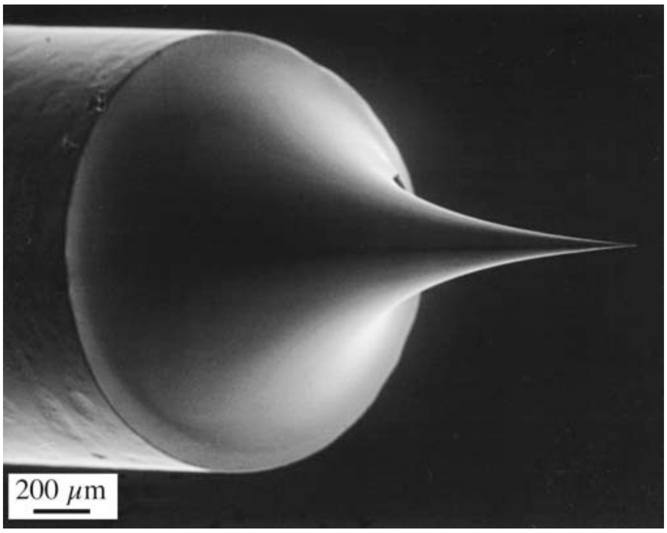

Figure 2.1: Image of a fine FEG tungsten tip [24]

sources have the disadvantage of lower stability. This means that the beam current fluctuates over time. FEGs allow the highest brightness of about $10^9\,\mathrm{A\,cm^{-2}\,sr^{-1}}$ among the three kinds of electron sources that were mentioned, but suffer from the lowest stability. Furthermore, the energy spread is predominantly ruled by the electron gun and defines the temporal coherency of the electron beam. For electron sources with a wide energy spread, monochromators may be utilized, however, the energy spread of FEGs reaching 0.2 eV is small enough to make this unnecessary for all applications in this work. The electron energy spread is particularly important in high energy-resolution EELS. A fine FEG tungsten tip is shown in Figure 2.1. FEGs consist of such a tip, the cathode, and two anodes. One anode is positively charged by several kV and this extraction voltage is responsible for the field emission in the tip. The second anode accelerates the electrons to the intended energy. The acceleration voltage is referred to as High Tension (HT). The emission current decreases with time because of contamination, even under UHV conditions. When contamination prevails, flashing the tip becomes necessary. See also, chapter 5 in [24] and chapter 2.4.1 in [25].

2.2 Electron Optics

To receive a microscopical image in a TEM, the electron rays emitted by the FEG must undergo two fundamental actions - forming an image of an object and focusing parallel rays to a point. In a light microscope the refraction in glass lenses is exploited in order to do so. Electron optics are based on the Lorentz force, which allows very similar ray paths, but also introduces a few fundamental differences. These are, among others, a rotation of electron rays around the optical axis that is associated with the nature of the Lorentz force, and an adjustability of those lenses. In contrast to glass lenses that have a fixed focusing strength and need to change their position to control their action on light rays, electron lenses in TEMs are fixed at their position and can change their strength by adjusting the current running through them. One great difference between these two kinds of lenses is that glass lenses nowadays are near-perfect. Electron lenses, on the other hand, struggle with inevitable aberrations because of fundamental properties of the electromagnetic field [26]. These aberrations are the de facto limitation of the performance of electron lenses. Apertures allow control over divergence and convergence of electron rays and thereby limit aberrations. Furthermore, the beam current can be regulated. Generally, electron lenses in TEMs are thin and their scattering angles are small. As explained in section 2.1, the electron source gives a lower limit for a TEM's resolution. To reach this limit, the electron lens setup must be optimized.

In principle, electron lenses act like glass lenses. Rays that penetrate the middle of the lens remain unaffected, while those that are near the optical axis are scattered weakly and those far strongly. The focal plane is the plane where rays that are parallel initially intersect. Focal length decreases for increasing lens strength. On the focal plane, the diffraction pattern can be imaged. It gives a location-independent angle-dependent pattern that looks like the sample structure's fourier transform. The image plane is where a real image of an object can be detected. Virtual images do not play a role in TEM. To reach high magnifications, several lenses are arranged in a way that the image plane of one lens is the object plane of the following, just as multiple lens compounds in light microscopes. Magnification is not limited, however, resolution defines the information limit that can be reached. As for glass lenses, the direction electrons take through lenses is arbitrary, both result in the same trajectory. For TEMs, the electron source is commonly on top of the device and facing downward. While the positioning of the electron source is reverted in STEMs, the orientation of the lens compounds is the same.

Electron lenses consist of two parts that can be seen in Figure 2.2. Firstly, there is the polepiece that is a soft iron core with a hole in it, called 'bore', and secondly, coils, commonly out of copper, that surround the polepieces. Most lenses feature two polepieces and the distance between them is called 'gap'. The bore-to-gap-ratio determines the strength of the lens. A power supply passes a current through the coils that creates the magnetic field in the bore. This magnetic field is axially symmetric, but inhomogeneous along the optic axis. As the coils also exhibit resistive heating, cooling of electron lenses is required. The local magnetic field strength and its orientation define the resulting electron paths.

As previously mentioned, performance limits of electron lenses are given by lens aberrations, especially regarding resolution. There are two main types, namely geometric and chromatic aberration. The most important geometric aberration is spherical aberration. The following paragraphs give an overview about spherical and chromatic aberration.

Spherical aberration refers to a lens defect that exhibits different focal lengths for rays off the optical axis than for those near it. Normally, this means that rays further off-axis are bent towards the axis more strongly or to increase the curvature of an incident spherical wavefront, respectively. This makes the image of a point object appear as a disk with high intensity in its center and decreasing intensity around. The radius of the

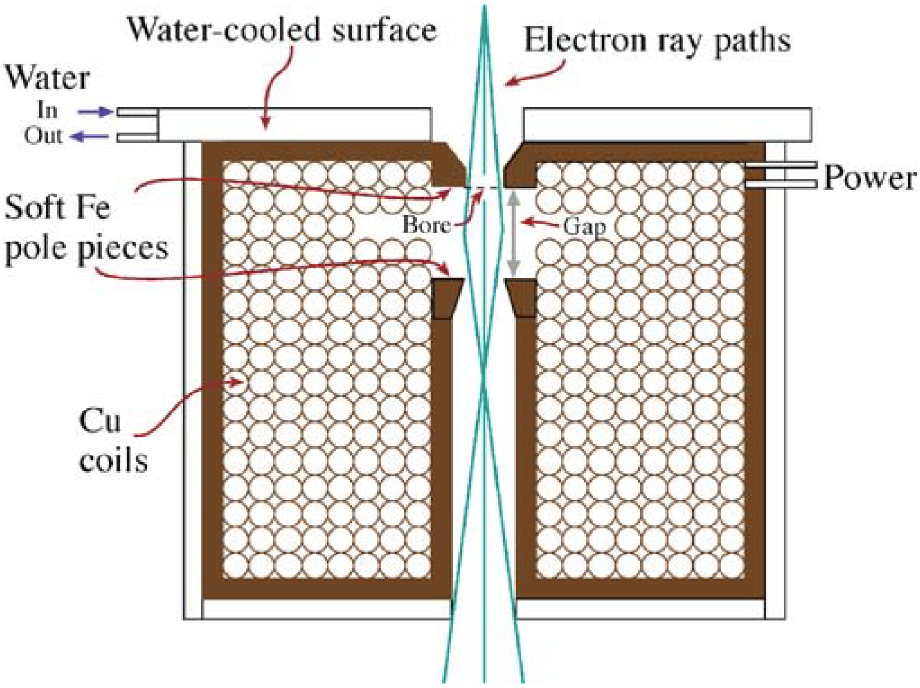

Figure 2.2: Systematic setup of a magnetic lens [24]

disk is

$$r_{sph} = C_s\beta^3 \tag{2.1}$$

where C_s is the spherical aberration coefficient, that, in case of not corrected TEMs, has the magnitude of the focal length, a few mm. β is the largest collection angle of the objective lens aperture. In a TEM, spherical aberrations of the objective lens are most critical to resolution, while in STEMs those in the condenser lens are just as important to be reduced because it forms the small probe with high current. Most often, spherical aberrations are those that after aberration correction still limit a TEM's resolution. In order to reduce spherical aberrations, a corrector must be introduced that diverges off-axis rays so that they are focused on the Gaussian-image plane. This corrector consists of a complex system of quadrupole and hexapole or octupole lenses and is computer-controlled. Because of the complexity of such correctors, particular electron trajectories will not be examined further. Two systems to correct spherical aberrations are the Nion corrector utilizing several quadrupole and octupole lenses and the CEOS system that consists of hexapoles and transfer lenses. These correction measures allow a change of the spherical aberration coefficient C_s, therefore, a decrease of the size of the disks from equation 2.1 and correspondingly enhanced image quality and resolution.

In section 2.1, it is mentioned that electrons emitted by a source have an energy spread. As the Lorentz force is dependent on the velocity of charged particles, electromagnetic lenses are sensitive to electron energy. The resulting effect is called chromatic aberration. The energy spread of cold FEGs is around 0.3 eV and the spread induced by the instability of power supplies, in comparison, can be neglected. The magnitude of this spread leads to aberrations that do not affect image resolution as long as spherical aberrations are not corrected. If corrected, chromatic aberrations are next to be compensated. Besides lens induced chromatic aberration, thick samples enhance electron energy dependent image quality loss. However, for 2D materials like graphene, these effects can be neglected. Similar to spherical aberration, chromatic aberration leads to the formation of disks on the Gaussian-image plane instead of point images. The radius of disks caused by chromatic aberrations follows equation 2.2:

$$r_{chr} = C_c \frac{\Delta E}{E_0} \beta \tag{2.2}$$

where C_c is the chromatic aberration coefficient, ΔE the energy spread, E_0 the beam energy or HT and β the largest collection angle. See chapters 6 and 9 in [24].

2.3 Electron-Sample Interaction

This section gives an overview about the interaction between the electrons that are emitted from the electron gun, passing through various electron lenses and penetrating the specimen. It is, therefore, a basis for section 2.4 about electron detectors. Figure 2.3 shows four categories of scattered electrons that occur when irradiating a thin sample.

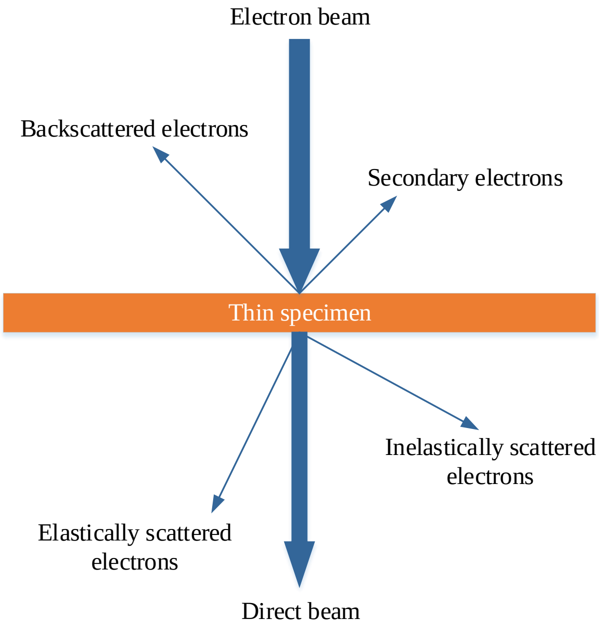

Figure 2.3: Illustration of electron-sample interactions with a thin specimen, self-created according to [24]

EM relies on Coulomb interactions between electrons from the electron source and the specimen, which is called electron scattering. Generally, these electron-sample interactions can be divided into elastic and inelastic. Elastic scattering refers to interactions that conserve the electron's kinetic energy, while for inelastic scattering the energy is decreased. Elastically scattered electrons contain essential information about the crystallography of the sample. For larger scattering angles, the amount of scattered electrons decreases strongly. Hence detectors are placed at small angles, as the measured intensity is high. Inelastically scattered electrons comprise valuable structural and chemical information about the specimen, e.g. as they lose energy during the scattering process. This is utilized in EELS. Furthermore, they are responsible for the beam damage inflicted upon the specimen, which is commonly sought to be minimized. See also, chapters 2, 3 and 4 in [24].

2.4 Electron Detectors - STEM and EELS

Regarding image analysis, processing, enhancement, display and storage of microscopy data, the digital format is superior to the analog one. Therefore, STEM data is usually acquired as a two dimensional array of contrast values. The scanning process is the origin of the pixels of this non-static image. The forward scattered electron detectors in a STEM, that this section is about, are in the viewing chamber, just like in a TEM. A measure for their quality is the Detection Quantum Efficiency (DQE) that is defined as $DQE = (\frac{SNR_{out}}{SNR_{in}})^2$. The optimal value of the DQE is 1.

In order to detect electrons, a scintillator-photomultiplier system (photomultiplier = PM) can be utilized. When electrons hit the scintillator, photons are emitted. A PM amplifies them, often reaching gains of the order of 10^8. These photons are then being detected and measured as an electric signal, which is the output of the PM. The DQE of scintillator-PM systems is typically about 0.9.

Electron detectors can be distinguished by their geometry and, correspondingly, how strongly scattered electrons they are meant to detect. Detectors that are placed in the direct beam, i.e. the ray of electrons that is parallel to the direction of the incident beam, are called bright-field (BF) detectors. This covers angles of about 0-40 mrad. Detectors may also be built in annular form, where the direct beam goes through the detectors hole and only scattered electrons are measured, making it a dark-field (DF) or annular dark-field (ADF) detector. They can be divided into detectors measuring medium (MAADF), approximately 40-80 mrad, and high angles (HAADF), approximately 80-200 mrad. The higher the scattering angle is, the lower is the amount of electrons scattered. This means that the intensity measured by a HAADF detector will generally be lower than measured by the MAADF detector. However, specimen atoms with higher atomic number Z show an increased probability of scattering electrons at higher angles. Hence the Z-contrast-dependency of HAADF detectors is generally higher than the one of MAADF detectors. For HAADF detectors the dependency is usually around Z^2.

Electron Energy Loss Spectroscopy (EELS) refers to the measurement of the energy distribution of electrons. It is capable of reliable elemental identification at near-atomic resolution. Furthermore, EELS allows spectrum imaging, which is a technique that creates an image with an EEL spectrum at each pixel. The low-loss region of an EEL spectrum contains electronic information about the sample, while for elemental data and information about bonding and atomic distribution the high-loss region of the spectrum

(>50 eV) needs to be considered. Every element has its characteristic EELS peaks. For example, nitrogen has one edge at an energy loss of 401 eV[1]. An EEL spectrometer is a magnetic prism that is mounted on the STEM after the post-specimen detectors. It disperses the incoming electrons in energy, which are then projected onto a CCD detector. The maximum achievable energy resolution of these spectra is governed by the electron source. In case of a cold FEG, it is about 0.3 eV. For elemental identification, an energy resolution of about 1.0 eV is sufficient.

Another kind of electron detector that is also sensitive to visible light are charge-coupled device (CCD) cameras. These are metal-insulator-silicon devices that store charge that is generated by the photons a scintillator emits as a result of the incident electron signal. CCDs consist of millions of such isolated capacitors and are the norm for TV recording of EM images. After accumulation of signals, all capacitors need to be read out which delivers an array of analog values. These can then be digitized and displayed. One further electron detector should be mentioned here. A Faraday cup captures all charged particles and the measured current is the same as the electron (or ion) beam current. See also, chapters 7, 22 and 37 in [24].

---

[1] http://www.eels.info/atlas/nitrogen

Chapter 3

State of the Art

3.1 Simulation

In this section, the simulations in [13] are reviewed to serve as a theoretical background. In the work, molecular dynamics simulations and density-functional-theory total-energy calculations were utilized in order to simulate low-energy boron and nitrogen ion irradiation of finite-size graphene sheets. The ion beam is assumed to be perpendicular to the graphene sheet as it will be the case in the experiments conducted in the context of this thesis. Further details regarding assumptions that were made can be found in the paper.

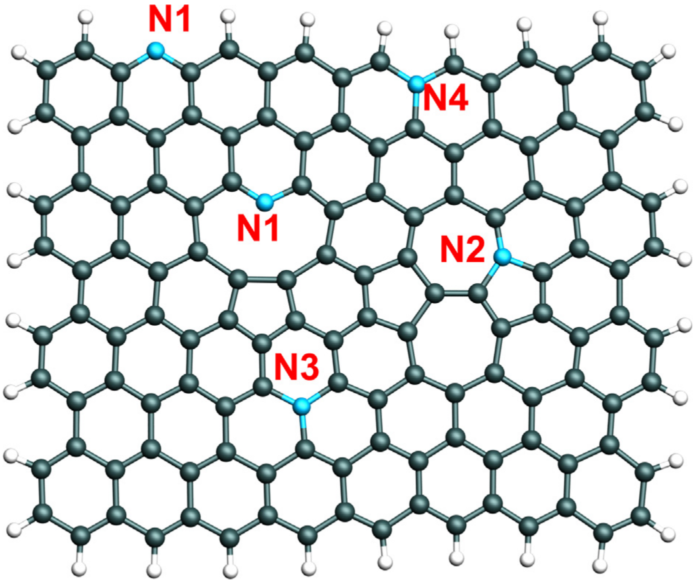

Figure 3.1: Nitrogen doping species in graphene, N1 showing pyridinic N, N2 pyrrolic N, N3 graphitic N and N4 graphitic "valley" N [27]

At first, a close look is taken at substitution processes. The focus of this work is on nitrogen implantation. Hence dopant ions are considered to be nitrogen. There is perfect substitution, which refers to a nitrogen ion having a large enough kinetic energy to be able to displace one carbon atom and subsequently being trapped at the original location of the carbon atom. Therefore, the ion is required to have few enough kinetic energy left over after the collision in order to be incorporated into the graphene lattice. This process leads to graphitic nitrogen. Figure 3.1 illustrates various N-doping sites. There is graphitic, pyridinic and pyrrolic N. Graphitic N refers to a structure including three sp^2 C-N bonds and pyridinic N to two sp^2 C-N bonds in a hexagon, while pyrrolic N indicates two C-N bonds in a pentagon and is sp^3 hybridized [27, 28]. Figure 3.2 shows the ion-energy-implantation-probability-function for perfect substitution. For nitrogen, a maximum substitution probability of 55% at an ion energy of 50 eV is predicted. Substitution probabilities of more than 10% are expected as long as the ion energy stays between 40 eV and 105 eV. For lower and higher energies, perfect substitution becomes increasingly insignificant.

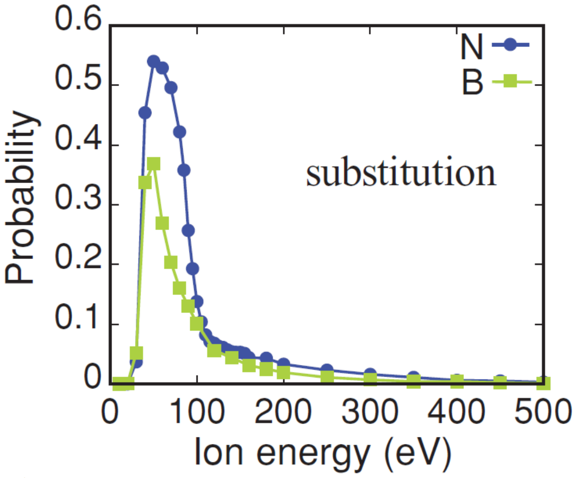

Figure 3.2: Dependency of perfect substitution probability on particle energy of nitrogen ions (blue) in graphene [13]

The paper focuses on what processes take place and how probable they are depending on ion energy. They include ejection of one or two carbon atoms and subsequent capturing of the dopant ion as well as creation of a single vacancy (SV), double vacancy (DV) or adatom.

It is possible that the incident ion displaces two carbon atoms and then remains in one of their positions. This results in pyridinic configurations, see Figure 3.1, in which the dopant forms two bonds with carbon atoms in the graphene lattice. The probability of this process to take place is shown in Figure 3.3. It is generally much lower than for perfect substitution. Also, the ion energy, at which the probability is high, is larger, which is intuitive, as two carbon atoms must be displaced. At the optimal energy for perfect substitution to occur, 50 eV, the probability for a substitution along with a SV to be created is slightly less than 1%, while it is 55% for perfect substitution. The highest

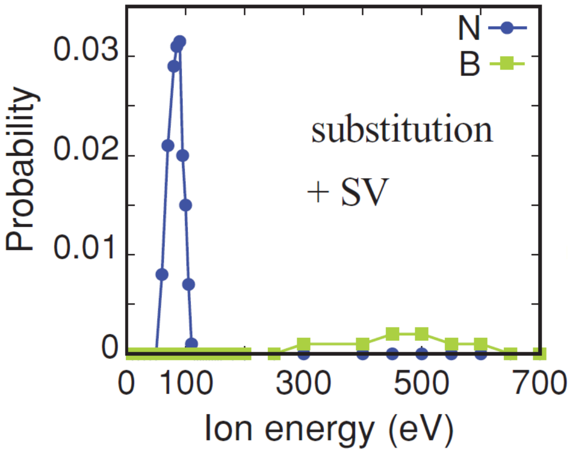

Figure 3.3: Probability of creation of pyridine-like N (blue) defect through introduction of a DV and subsequent capture of ion with respect to its original energy [13]

probability for pyridinic nitrogen to be created is around 3%. Mechanisms leading to pyrrolene-like structures are imaginable as well. These have not been observed in this work, though.

Besides desired substitution processes, low-energy ion irradiation may cause defects in graphene, most likely SVs. The probability for SVs to be created at a nitrogen ion energy of 50 eV is expected to be as low as a few percent. However, for higher ion energies, this probability strongly increases up to 55% at 125 eV. Another frequently created defect were DVs. Since the threshold for displacing a carbon atom is around 22 eV, the probability for DVs to be created at the optimal ion energy for perfect substitution using nitrogen, 50 eV, is practically zero. From around 60 eV it increases up to a maximum probability of 16% at 110 eV ion energy. For explanations on substitution and defect creation mechanisms, see [13].

For very low energies, the most probable process to take place is the generation of an adatom. For energies near zero, the probability naturally is close to 1. It decreases with increasing ion energy, being in the range of 20-25% at 50 eV and reaching near-zero values at 85 eV. Migration barriers of about 0.1 eV to 1.1 eV allow them to move nearly freely on the graphene surface. The creation of nitrogen adatoms does not have a direct relevance to the focus of this thesis, as nitrogen adatoms are expected to evaporate over time. As long as they have not, migration barriers of about 0:1 eV to 1:1 eV allow them to move nearly freely on the graphene surface. Carbon adatoms, however, are expected to fill pyridinic doping sites, resulting in graphitic N and lowering the overall share of pyridinic nitrogen.

3.2 Experimental

Nitrogen doping of graphene can be achieved and the resulting structure analyzed in many ways. There are postsynthesis and during-growth methods, including direct growth of N-doped graphene layers and addition of nitrogen gas during growth [29]. An after-growth chemical process is post-annealing under a N-containing atmosphere [30]. However, these chemical processes may lead to undesired contamination and offer low controllability over the creation of pyridinic and pyrrolic doping sites [29]. An alternative postsynthesis method is the utilization of accelerated nitrogen ions from a plasma to irradiate graphene. This approach is routinely used to manufacture conventional semiconductor devices and has the advantage to be spatially selective and allow doping to take place when the sample is already in a device [27]. In order to apply a similar method for doping graphene, a deep understanding of the processes on atomic scale is necessary, as the response of atomically thin graphene to ion irradiation is significantly different from three-dimensional materials [13].

Besides different approaches concerning the doping process, there are two kinds of graphene samples one can work with in order to investigate graphene doping. On one hand, there are studies trying to comprehend implantation mechanisms in graphene on a substrate of any kind [29, 31–34]. On the other hand, suspended free-standing graphene samples are examined [14, 27, 28, 35]. While experimenting with graphene on a substrate is more closely related to potential applications, investigating free-standing graphene offers a more fundamental understanding of the material. Also, the sample preparation method may have an impact on results. CVD grown graphene offers high quality SLG on large areas, making it optimal for microscopic observation. Free-standing SLG, in comparison to bi- or multilayer graphene [27], is the most basic sample setup and, therefore, appropriate for an investigation as fundamental and unperturbed as possible.

The standard technique for studying N-doped graphene is X-ray photoelectron spectroscopy (XPS). It allows a quantitative measurement of bonding configurations [16]. However, as XPS has a limited spatial resolution, defect structures cannot be directly derived [28]. Also used for characterizing N-doped graphene is Raman spectroscopy [16]. This method permits the quantification of defects caused by nitrogen implantation, the doping level and electron concentration. A technique that is able to measure electronic properties and structure of N-doped graphene with atomic resolution is scanning tunneling microscopy (STM) [16]. It can identify single nitrogen atoms and their defect configurations. Quantification of the doping level may prove difficult, though. A combination of STEM and simultaneous EELS as another alternative offers the possibility to directly image doping defect structures and bonding configurations, while being able to distinguish elements atom-by-atom via contrast variation of the annular dark-field (ADF) [36] and quantify the amount of nitrogen atoms implanted into the graphene lattice [28].

In the following, a few studies about nitrogen doping of graphene using ion irradiation are presented. Two papers [27, 33] demonstrate an advantage of plasma treatment approaches. In contrast to doping processes during CVD, which usually reach

2-3 at.% [14, 16], although 8.9 at.% [37] and 16 at.% [38] have also been reached, using nitrogen ion plasma high nitrogen doping densities of up to 20 at.% are achievable. This is valid for both graphene on top of a substrate as shown in [33] and suspended graphene [27]. In case of suspended graphene, exfoliated few-layer graphene flakes and CVD-synthesized SLG were irradiated. XPS, SEM and STEM were utilized in the investigation. A common electron cyclotron resonance (ECR) microwave plasma source was used. The ion acceleration is said to be set to 1.0 kV as extractor voltage is -0.2 kV and anode at 0.8 kV. However, it remains unclear if these two can simply be added to determine the ion energy. The irradiation took place under a chamber pressure of 1×10^{-4} mbar and consisted of a 5 min followed by a 15 min treatment. The analysis was done in a 10^{-10} mbar ultra-high vacuum (UHV) environment. After irradiation, the samples underwent two annealing steps, one at 250 °C and the other at 430 °C for 15 min each.

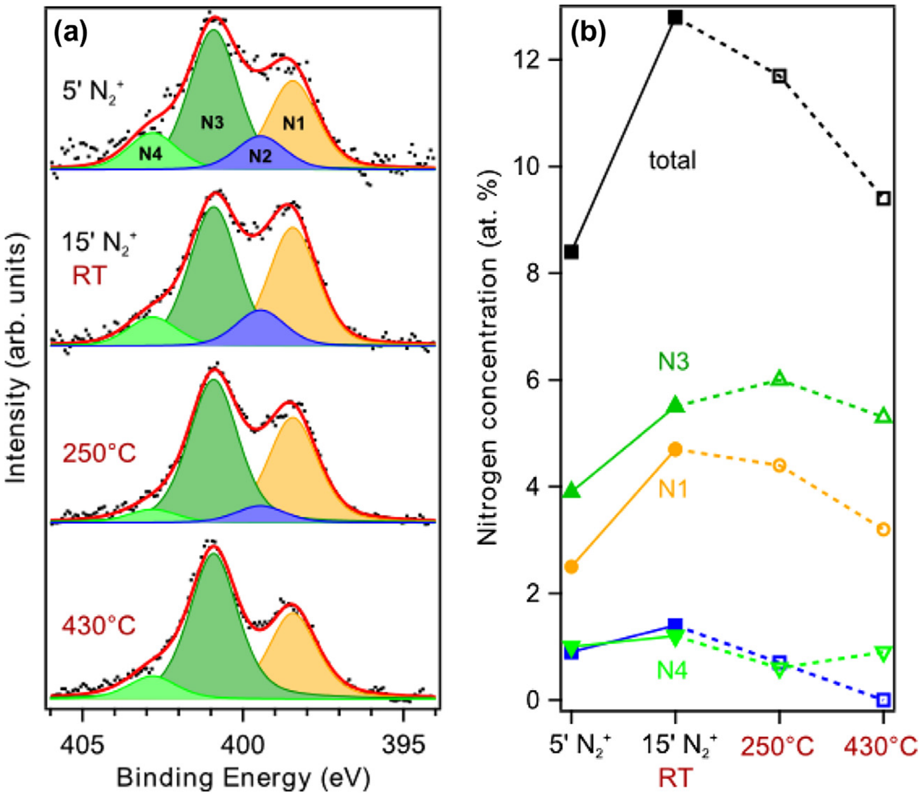

Figure 3.4: XPS-spectra including relative occurrences (left) and concentration (right) of N-species after different treatment steps [27], area under peaks is proportional to occurrence (left), N1-4 according to Figure 3.1, N1 pyridinic, N2 pyrrolic, N3 and N4 graphitic

Figure 3.4 shows the XPS-spectra with the peaks of the four nitrogen species presented in Figure 3.1 after each of the four treatment steps, including two irradiation and two annealing steps. Also, the derived concentrations after each step are presented. As can be seen, after the first short irradiation step, graphitic nitrogen (N3 and N4) appeared to be the most numerous defect species with 3.9+1.0 at.% followed by its pyridinic counterpart (N1) with 2.5 at.%. Pyrrolic nitrogen (N2) reached a concentration of 0.9 at.%. A second, longer irradiation stage increased the overall nitrogen concentration of all four species. The concentrations were 5.5+1.2 at.% for graphitic nitrogen (N3 + N4), 4.7 at.% for pyridinic nitrogen (N1) and 1.4 at.% for pyrrolic nitrogen (N2). During annealing, the overall nitrogen concentration decreased, as implanted atoms either desorbed or diffused. This, however, had different impact depending on the defect species. Pyrrolic nitrogen is thought to be the least thermally stable structure. The clear decrease of concentration that was observed during both annealing steps approved this. Pyridinic and, especially, graphitic nitrogen are expected to be stable enough to stay unaffected even for temperatures of the order of 1000 °C, however, a decreasing concentration has been observed for pyridinic species as well. Further experiments have shown that for exfoliated graphene samples qualitatively equivalent results are achieved. Also, in order to reach even higher doping concentrations of up to 20 at.%, longer irradiation times of around 90 min were necessary in this setup. After this time, saturation effects emerge and prevent further doping. Furthermore, it was noted that doping concentration and irradiation time are not proportional in this study. The speed of nitrogen concentration increase slowed down over time. However, with another kind of plasma treatment a linear dependency has been shown [33].

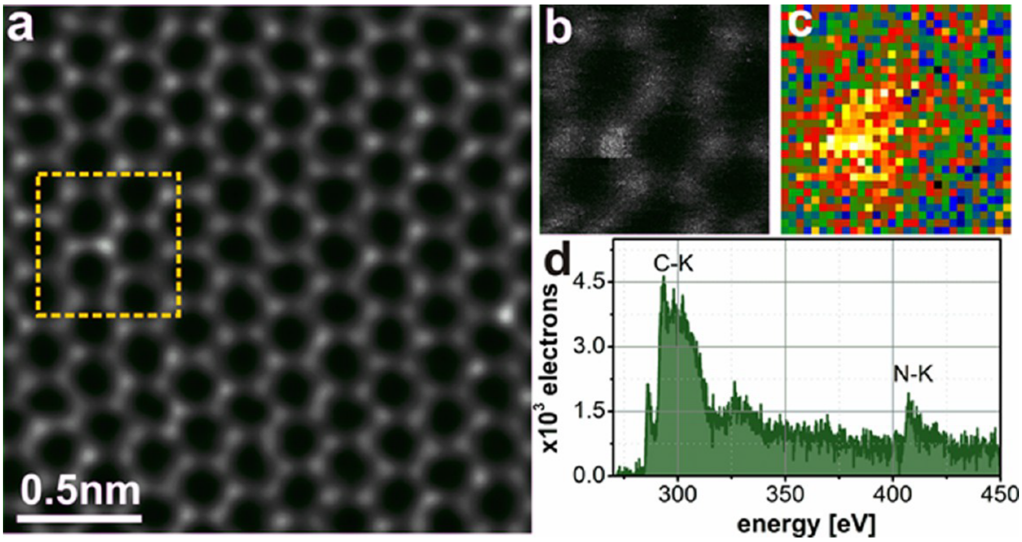

Figure 3.5: (a) Double Gaussian filtered atomic resolution HAADF image of graphitic N, (b) raw HAADF image of area marked in a, (c) corresponding spectrum image in energy window 400-420 eV, (d) sum of EEL spectra from pixels around N atom [35]

The findings of Åhlgren et al. [13], that serve as a theoretical background for the experiments executed in this thesis, have already been experimentally verified to some extend by Bangert et al. in [35]. Therefore, an overview about their setup and results is given. Free-standing SLG and few-layer graphene were irradiated by B- and N-ion plasma with ion energies between 20 and 200 eV in a single step without subsequent annealing. To reach such low energies as 25 eV, a system that decelerates high-energy N ions to these energies has been employed. Samples were analyzed by a Nion VG HB501 and Nion UltraSTEM 100 with electron energies of 80 keV and 60 keV, respectively.

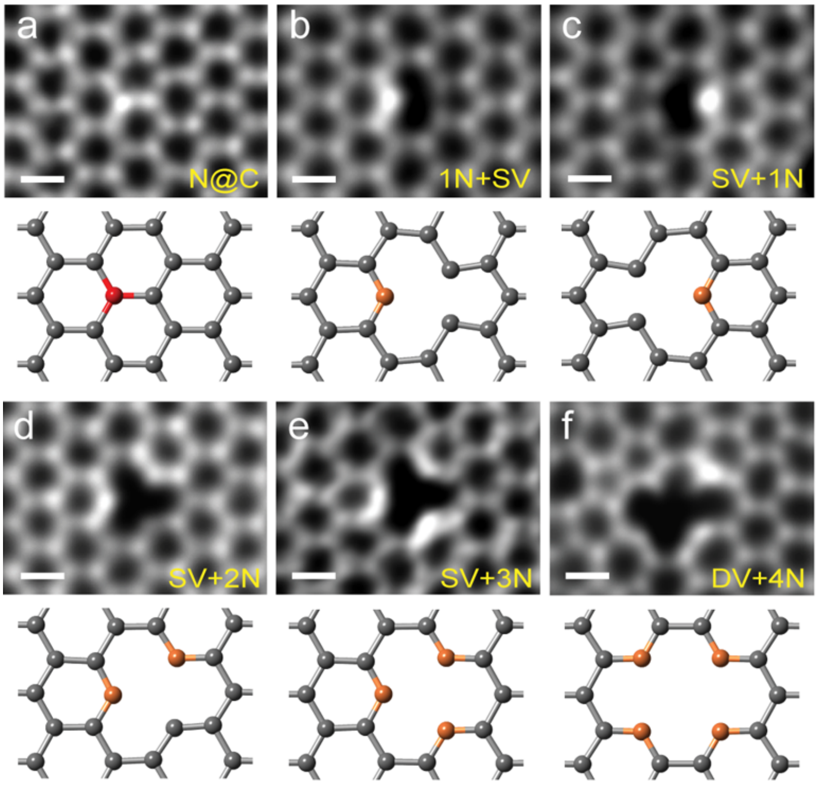

Figure 3.6: One graphitic and five pyridinic N doping sites and their corresponding atomic models [28]

The second of these STEM and EELS systems is the same type of device that will be used for analyzing the samples produced in the following experiments, see section 4.2. For ion energies between 100 and 200 eV, it was found that the doping level of SLG regions was very low. Only thicker areas were able to decelerate these ions to energies that allowed them to be trapped and implanted. Multilayered and contaminated regions were noticed to have significantly higher concentrations. Experiments employing irradiation with an ion energy of 25 eV have proven to be appropriate for efficient N-doping of graphene. The contrast difference between C atoms and B and N atoms in the HAADF images was following the expected Z^2 dependency, see section 2.4. The contrast difference was evaluated statistically and allowed automatized distinction between C and N atoms. However, it was also found that the deviation ($\approx 2\sigma$) of the contrast of carbon atoms was $\approx 20\%$. Figure 3.5 shows a HAADF image of a graphitic nitrogen spot and the corresponding EEL spectrum. The EEL spectrum clearly identifies the suspected atom as nitrogen. Stability of the implanted ions under the electron beam was shown as they stayed in the same lattice positions during repeated STEM scans. A doping level of

$\approx$ 1% was measured, while the distribution of N atoms appeared to be nonuniform. The alternative approach proposed in [13] to use higher energy ions to create defects and subsequently fill those defects during a low-energy irradiation step is said to be promising.

A similar experiment is presented in [28]. Method of analysis was a combination of STEM and atomic EELS, as previously. In this case, a mixture plasma of ozone and nitrogen was used to irradiate the sample. The ion energy is not known. A set of different binding configurations of implanted nitrogen atoms was observed. Figure 3.6 shows graphitic N and different configurations of pyridinic N, two SVs with one N implanted each, two SVs with two and three N implanted, respectively, and a DV featuring four N atoms.

The authors point out that the contrast of N atoms often varies, especially for pyridinic N, and one may have difficulties to ensure the existence of single N atoms. There are no specific doping concentrations given in the paper, however, it is mentioned that 60 SVs were found in a region of $2500\,\mathrm{nm}^2$ and most of those would contain N atoms. This would correspond to a low pyridinic N concentration of around 0.1 %, assuming that there are 1.5 nitrogen atoms per SV. It is also stated that graphitic N doping could not exceed concentrations of a few at.%, while pyridinic N could also exist with higher local N densities [39, 40]. For applications that require high doping densities, pyridinic N doping may, therefore, be significant.

3.3 Aims and Approach

This section, firstly, formulates central aims of this work and, secondly, gives a short summary of all information directly relevant to the experiments that are conducted. Therefor findings from sections 3.1 and 3.2 will be recapped and their meaning for the experiments reasoned.

The paramount ambition of this thesis is to provide direct, atomic resolution STEM images of N-doping sites in suspended SLG. The experimental process will show whether the difference in contrast between C and N atoms is sufficient to identify nitrogen atoms in these STEM images or not. If not sufficient, single-atom EELS can be utilized to classify N atoms. EELS is also supposed to determine doping concentrations if possible.

In order to observe nitrogen atoms inside the graphene lattice, graphene samples must be treated with nitrogen plasma first. This will be done with a commercially available UHV compatible microwave ECR plasma source. Graphene coated TEM grids were purchased from Graphenea Inc. The experiment will not be carried out in situ, i.e. in the microscope. However, the experimental setup allows the uninterrupted transport of samples between irradiation chamber and microscope in UHV. This may prove useful to avoid unwanted contamination.

Because of the complexity and inconsistency of experimental results, the outcome of the simulations in [13] is used to determine the ion energy range and optimum that the plasma source should be operated with. An energy range that is expected to deliver good results was mentioned in section 3.1. In the range of approximately 40 to 105 eV the probability for perfect substitution and the ensuing creation of graphitic nitrogen are sufficiently high, supported by the findings in [28]. The optimal energy is 50 eV, while slightly higher energies may be required for the effective creation of pyridinic doping sites. The expectations that arise from the simulations are that graphitic doping sites are predominant, while pyridinic and pyrrolic N appears seldom or never. Pyridinic N appears more frequently than pyrrolic N according to [27]. If the samples go through an annealing step after the irradiation, it is expected that the results are directly influenced, namely, depending on temperature, a strong decrease of pyrrolic N sites and a slight decrease of overall N-doping concentration. Longer irradiation time does not necessarily help to significantly increase the doping level. Furthermore, following [13, 28], the expected doping concentration is in the magnitude of 10-50% of the ion dose, as long as no saturation effects show up and the created doping sites are stable. SVs are expected to be the most frequent kind of defect. Whether the contrast difference between C and N is large enough to distinguish them remains to be seen, as different observations are to be found, e.g. in [35] and [28]. For the analysis, the electron microscope will be operated with a HT of 60 kV. This is safely below the carbon displacement threshold at around 85 keV [41], which limits radiation damage. It must be noted that the available plasma source may not be optimal for low- and very-low-energy plasma treatments, e.g. compared to the 25 eV plasma source in [35]. Also, as applications that require high doping concentrations supposedly depend on pyridinic N [28], it may be worthy to not only focus on perfect substitution but also the creation of SVs along with substitution.

Chapter 4

Experimental Setup

4.1 Sample Preparation

The aim of the experiments related to this thesis is to use a plasma source to implant nitrogen into the graphene lattice. However, as this was not trivial to achieve, the first part of this section is dedicated to point out major problems that arose during the experiments and how they can be solved to an extent that the purpose of this work is fulfilled. A short overview of all difficulties that were encountered during the experiments is given in section 6.1. The second part is about the setup that is able to produce the results that are presented in chapter 5 and what values the parameters are set to. Also, three estimates of the ion dose are presented.

The plasma source used for the ion implantation is the MPS-ECR model from SPECS Surface Nano Analysis GmbH in hybrid source mode. It uses a microwave discharge to ionize gas atoms and generate a plasma. Apertures with different diameters in mm range define the neutral particle flow out of the source under vacuum conditions. Charged particles are pulled out of the plasma chamber by an extractor electrode and then accelerated by an anode. The associated power supply shows and allows control over magnetron, extraction and anode voltage and current. The magnetron current I_{magn} determines the intensity of microwaves penetrating the gas in the plasma chamber and thereby the amount of ions generated per unit time. It is suggested to be around $15\,\mathrm{mA}$. The anode voltage U_{an} is set to the desired beam energy, which is $50\,\mathrm{eV}$, and the extractor voltage U_{extr} is suggested to be set to $-200\,\mathrm{V}$. However, it should not exceed U_{an}. Therefore, U_{extr} is set to the minimum, which is $-50\,\mathrm{V}$, in the first setup. In order to ignite a plasma, nitrogen is supplied through a gas line. A leak valve controls the gas flow into the chamber and, therefore, the plasma chamber pressure p_{ch}. The target chamber is pumped by a turbo molecular pump. p_{ch} is the fourth parameter being relevant to the plasma source operation and is directly dependent on the target chamber pressure p_t. They are suggested to be at the lowest level at which the source is in stable operation. As the plasma chamber pressure p_{ch} is not measured directly in the setup, the target chamber pressure p_t is considered. The samples used in the experiments are commercially available Graphenea, which are suspended SLG samples. The graphene layer is on top of a thin carbon foil that has circular holes, which contain the suspended graphene. A gold grid holds the carbon foil. A few exfoliated graphene samples were produced and irradiated as well.

Several experiments with a simple setup, consisting of the above described plasma source and the sample in its holder, were carried out under various plasma source properties. The governing parameters of the plasma source, namely I_{magn}, U_{an}, U_{extr}, p_{ch} and p_t, respectively, were varied only slightly and kept close to their standard values. In this simple setup, the magnitude of the ion dose rate n was quantified through voltage measurement at an isolated flange. The dependency of n on the four plasma source parameters was measured. However, besides a hysteresis that was observed for the p_t-n-relation, conducting the same experiment twice under the same conditions regularly leaded to very different results regarding n. This either means that this way of measuring n is not reliable or that the plasma source's operation is not clearly determined by a certain set of values for I_{magn}, U_{an}, U_{extr} and p_t. If these four parameters do not define the plasma sources operation, a consistent operation of the source may not be possible with this kind of setup.

Another parameter that is essential for the operation of the plasma source is the time that the sample gets irradiated. As a basis for determining a good irradiation time the ion dose measurements were used. It is expected that possible effects on the sample are in the same order of magnitude or one lower than the ion dose it gets exposed to, based on the substitution and defect creation probabilities postulated in [13]. This refers particularly to defects that the ion bombardment causes. The time that is needed to reach an ion dose of $1\,\mathrm{nm}^{-2}$ is calculated as doping in this order of magnitude is desired. Table 4.1 introduces the variables that occur in the calculation.

Table 4.1: Variables in Flange Ion Dose Calculation

Symbol	**Description**	**Unit**
N_{flange}	Average ion dose on flange	nm^{-2}
n_{flange}	Average ion dose rate on flange	$\mathrm{nm}^{-2}\,\mathrm{min}^{-1}$
t_{irr}	Irradiation time	min
n	Ion dose rate	$\mathrm{nm}^{-2}\,\mathrm{min}^{-1}$

Parameters that are given or measured are to be found in Table 4.2 and further relevant setup parameters are shown in Table 4.3. N_{flange} is calculated as following

$$N_{flange} = n_{flange} \cdot t_{irr} \tag{4.1}$$

where

$$n_{flange} = \frac{I_{flange}}{e \cdot A_{flange}} \tag{4.2}$$

Inserting n_{flange} from equation (4.2) into equation (4.1) and rearranging leads to

$$t_{irr} = \frac{N_{flange} \cdot e \cdot A_{flange}}{I_{flange}} \tag{4.3}$$

As

$$\frac{N_{sample}}{N_{flange}} = (\frac{a_{flange}}{a_{sample}})^2 \tag{4.4}$$

equation (4.3) can be expressed as

$$t_{irr} = \frac{N_{sample} \cdot e \cdot A_{flange}}{I_{flange}} \cdot (\frac{a_{sample}}{a_{flange}})^2 \tag{4.5}$$

Table 4.2: Given and Measured Values for Flange Ion Dose Calculation

Symbol	**Description**	**Value**
I_{flange}	Ion current on flange	$0.01\,\mu\mathrm{A}$ [2]
e	Elementary charge	$1.6 \cdot 10^{19}\,\mathrm{A\,s}$
A_{flange}	Flange area	$15\,\mathrm{cm}^2$
N_{sample}	Average ion dose on sample	$1\,\mathrm{nm}^{-2}$
a_{flange}	Distance from plasma source aperture to flange	$18\,\mathrm{cm}$
a_{sample}	Distance from plasma source aperture to sample	$6\,\mathrm{cm}$

Inserting the parameter values from Table 4.2 into equation (4.5) results in

$$t_{irr} = 3 \cdot 10^3 \mathrm{s} = 50\,\mathrm{min}$$

The corresponding ion dose rate n is calculated as

$$n = \frac{N_{sample}}{t_{irr}} \tag{4.6}$$

That is

$$\boxed{n = 2 \cdot 10^{-2}\ \mathrm{nm}^{-2}\,\mathrm{min}^{-1}}$$

This calculation is based on a few assumptions and approximations. Firstly, the voltage difference between the flange and ground devided through the resistance of the voltmeter is assumed to give a good measure of the real ion current. Secondly, for simplicity, ion doses and dose rates are calculated as average over flange and sample area, respectively. The ion dose is expected to follow a Gaussian distribution, though. Thirdly, the distance-

---

[2] measured as $\approx \frac{0.2\,\mathrm{V}}{20\,\mathrm{M\Omega}}$

Table 4.3: Additional Setup Parameters (Flange)

Symbol	**Description**	**Value**
I_{magn}	Magnetron current	15 mA
U_{an}	Anode voltage	0.8 kV
U_{extr}	Extractor voltage	−0.2 kV
v_{pump}	Vacuum pump power	$50\,\mathrm{L\,s^{-1}}$
p_t	Target chamber pressure	$8 \cdot 10^{-6}$ mbar
d_{ap}	Aperture diameter	0.2 mm

ion-dose-relation is assumed to be quadratic. And finally, the above shown distances a_{sample} and a_{flange} could not be measured precisely and were, therefore, approximated. Also, the effective flange area A_{flange} could not be determined and is estimated. Taking all this into consideration, the results of the above shown calculation are expected to deliver at least the right magnitude of an appropriate time setting.

In order to backup the calculation result, another way of estimating the ion dose rate was used. The chamber pressure of the plasma source contains information about how many particles leave the source per unit time. These particles include atoms and ions, so the atom-to-ion-ratio has to be known. An approximate value of 10-20 % is provided by the manufacturer of the plasma source for this cracking efficiency.

The gas flow into the target chamber is equal to the gas flow out. Gas flow refers to the product of pressure and flow in volume per time. Equation (4.7) shows this relation and Tables 4.4 and 4.5 describe all involved parameters.

$$p_{gas} \cdot (n_{gas} \cdot A_{irr} \cdot \frac{V_M}{N_A}) = v_{pump} \cdot p_t \tag{4.7}$$

Table 4.4: Variables in Gas Flow Ion Dose Calculation

Symbol	**Description**	**Unit**
n_{gas}	Gas particle flow rate per sample area	$\mathrm{nm^{-2}\,min^{-1}}$
A_{irr}	Irradiated area	$\mathrm{nm^2}$
r_{irr}	Radius of irradiated area	mm
n	Ion dose rate	$\mathrm{nm^{-2}\,min^{-1}}$

As only a part of the particles leaving the plasma chamber are ions, the ion dose is calculated as follows

$$n = n_{gas} \cdot \eta \tag{4.8}$$

and the circular irradiated area is determined as

$$A_{irr} = \pi \cdot r_{irr}^2 = \pi \cdot a_{sample}^2 \cdot \tan^2(\alpha_{irr}) \tag{4.9}$$

Substituting n as given in (4.8) and A_{irr} following (4.9) in equation (4.7) gives

$$n = \frac{p_t \cdot N_A \cdot v_{pump} \cdot \eta}{p_{gas} \cdot V_M \cdot \pi \cdot a_{sample}^2 \cdot \tan^2(\alpha_{irr})} \tag{4.10}$$

Table 4.5: Given and Measured Values for Gas Flow Ion Dose Calculation

Symbol	**Description**	**Value**
p_{gas}	Gas line pressure	1500 mbar
v_{pump}	Vacuum pump power	$500\,\mathrm{L\,s^{-1}}$
V_M	Volume per mol at p_{gas}	$16\,\mathrm{L\,mol^{-1}}$
N_A	Avogadro constant	$6.0 \cdot 10^{23}\mathrm{mol}^{-1}$
p_t	Target chamber pressure	$3.2 \cdot 10^{-6}\mathrm{mbar}$
a_{sample}	Distance from plasma source aperture to sample	70 mm
α_{irr}	Largest irradiation half-angle	75...80°
η	Cracking efficiency	10...20%

Inserting the values from Table 4.5 into equation (4.10) results in

$$\boxed{n = 0.5...2.4\ \mathrm{nm}^{-2}\,\mathrm{min}^{-1}}$$

This second approach assumes a homogeneous ion dose over a circular area defined by a certain irradiation angle. Besides this, a fixed value for the cracking efficiency does not take the plasma source operation parameters into account. In fact, the ion dose is not linear to the chamber pressure at all. Instead, there is an optimal pressure where the ion dose is largest and higher chamber pressures lead to a decreasing dose. Another approximation is the irradiation angle α_{irr}, which has been calculated through extrapolation of known values for larger anode voltages. This appears to be imprecise, though. The calculated ion dose rate is two orders of magnitude higher than the previous calculation following equation (4.10) suggested. A factor of 10 is explained by a ten times larger vacuum pumping power than in the previous setup. The remaining discrepancy between this result and the previous one may be accounted to a larger irradiation angle than used in this calculation, a different cracking efficiency than stated or the faulty assumption of a homogeneous distribution of dose.

Table 4.6: Additional Setup Parameters (Gas Flow)

Symbol	**Description**	**Value**
I_{magn}	Magnetron current	arbitrary
U_{an}	Anode voltage	arbitrary
U_{extr}	Extractor voltage	arbitrary
v_{pump}	Vacuum pump power	$500\,\mathrm{L\,s^{-1}}$
p_t	Target chamber pressure	$3.2 \cdot 10^{-6}\,\mathrm{mbar}$
d_{ap}	Aperture diameter	$1\,\mathrm{mm}$

As the first calculation following equations (4.5) and (4.6) was considered more reliable, time settings in the magnitude of 1 h were chosen for this simple setup. However, using this setup, every manufactured sample faced strong contamination issues, also for short irradiation time settings. The coverage of the plasma-induced contamination is so high that continuously only clean spots with diameters of a few atoms could be found. Furthermore, this contamination cannot be removed by sample heating, which usually removes unwanted contamination, at least temporarily. The particles that are responsible for this contamination are supposedly bound at the vacuum system walls initially. Ion irradiation may then evaporate them. Because of the high amount of defects that the plasma creates on the specimen, these particles are likely to subsequently get bound by the sample.

No satisfactory results were achieved in a series of experiments in the simple experimental setup, only comprising the plasma source connected to the vacuum system pumped by a $50\,\mathrm{L\,s^{-1}}$ turbo molecular pump due to contamination problems. Therefore, a new assembly is realized. It offers several advantages, including a reliable measurement of the ion dose, an installed laser capable of heating the sample during the irradiation process, a ten times stronger $500\,\mathrm{L\,s^{-1}}$ turbo molecular pump and spatial separation from the microscope, allowing sample preparation to take place independent from microscope operation. This second setup features a target chamber that allows the turbo molecular pump to operate at a large surface, allowing the increased pumping speed. Also, several attachments can be added to the chamber. For example, to allow a precise ion dose measurement, a Faraday cup is attached. This solves the previous problem of finding an appropriate time setting for irradiation. Furthermore, constant laser heating during irradiation is supposed to limit contamination issues.

Table 4.7: Variables in Faraday Cup Ion Dose Calculation

Symbol	**Description**	**Unit**
n	Ion dose rate	$\mathrm{nm}^{-2}\,\mathrm{min}^{-1}$
$I_{Faraday}$	Ion current in Faraday cup	nA

Ion dose measurements using the Faraday cup shortly after the measurement, at the same location as the sample is irradiated, lead to the following result:

$$n = \frac{I_{Faraday}}{e \cdot A_{Faraday}} = \frac{U_{Faraday}}{R_{Fluke87} \cdot e \cdot A_{Faraday}} \tag{4.11}$$

Table 4.8: Given and Measured Values for Faraday Cup Ion Dose Calculation

Symbol	**Description**	**Value**
$U_{Faraday}$	Faraday cup voltage	$200\,\mathrm{mV}$
$R_{Fluke87}$	Internal resistance of Fluke 87	$10\,\mathrm{M\Omega}$
e	Elementary charge	$1.6 \cdot 10^{19}\,\mathrm{A\,s}$
$A_{Faraday}$	Faraday cup area	$28\,\mathrm{mm}^2$

Inserting the values from Table 4.8 into equation (4.11) results in

$$\boxed{n = 0.27\,\mathrm{nm}^{-2}\,\mathrm{min}^{-1}}$$

Table 4.9: Additional Setup Parameters (Faraday Cup)

Symbol	**Description**	**Value**
I_{magn}	Magnetron current	$16\,\mathrm{mA}$
U_{an}	Anode voltage	$0.05\,\mathrm{kV}$
U_{extr}	Extractor voltage	off
v_{pump}	Vacuum pump power	$500\,\mathrm{L\,s}^{-1}$
p_t	Target chamber pressure	$3.2 \cdot 10^{-6}\,\mathrm{mbar}$
d_{ap}	Aperture diameter	$1\,\mathrm{mm}$

In the series of measurements that were conducted, it has been noticed that unplugging the extractor anode can raise the ion dose rate by a factor of about five compared to when $U_{extr} = -0.2\,\mathrm{kV}$. The above shown result of the Faraday cup measurement was achieved with $U_{extr} =$ off. The result of this measurement is seen as the most significant among the three results that were obtained and presented, as it is the only direct measurement of the ion dose rate. Considering the first setup that the flange measurement was conducted with, theoretically, with a 50 times smaller ion dose rate, the Faraday cup measurement leads to an ion dose rate estimate that is around four times smaller. This discrepancy is sufficiently explained by geometrical uncertainties (A_{flange}, a_{flange}, a_{sample}, $A_{Faraday}$) and the fact that both measurements were conducted in different setups (U_{extr}, v_{pump}, d_{ap}). The measurement shows that the ion dose rate in the first setup was indeed low, which generally may make heating during irradiation troubling, as irradiation times are long, possibly damaging samples. In comparison to the gas flow calculation, the Faraday cup measurement suggests an ion dose rate that is slightly lower. This shows that the gas flow calculation can give a good approximation of the real ion dose rate, however, it does not take several important plasma source parameters into account. A separate, direct measurement of the ion dose rate may be useful, as it allowed a straight forward optimization of the plasma source increasing the dose by a factor of around 5 in the experiments. Together with the pumping speed, which is increased by a factor of 10, the ion dose rate is enhanced by a factor of about 50, comparing the first and last setup. Hence irradiation times are corrected to be smaller than previously. To reach the desired dose of $1\,\mathrm{nm}^{-2}$, only 4 minutes of irradiation are required.

A new problem had to be addressed to successfully irradiate samples in this second setup. The laser heating destroyed large parts of the sample when its power was too large, as the sample gets heated constantly over minutes. However, when the power is below a certain threshold, laser heating the sample does not have the desired effect and heavy contamination is the result. Therefore, a series of samples was made with the laser power being above the contamination threshold, while being far smaller than power settings that were able to damage the sample. The entire series of these specimens faced one problem: Whenever they were analyzed in the STEM that will be subject of section 4.2, no atomic resolution could be reached. As the laser does not cover the entire sample, CCD images along the border between the area that gets hit directly by the laser and the one that is only heated by the heat conductivity of the sample were able to explain this phenomenon. The carbon foil in the zone that was heated directly showed a clearly smaller contrast than the indirectly heated area. This means that the laser is able to thin down the carbon foil significantly, which is expected to enhance vibrations during microscopy, thus, impeding reaching atomic resolution. Therefore, the laser power was optimized to be as small as possible to still produce clean samples. Long irradiation times should be avoided to ensure specimen stability. An ion dose rate similar to the one determined by the Faraday cup measurement and equation (4.11) is required to keep irradiation and heating times short. Even short irradiation times and laser power being just above the contamination threshold thin down the carbon foil to an extent that vibrations in the microscope setup are too influential and do not allow atomic resolution.

Even sample areas that are close to the gold grid do not allow atomic resolution then. Because no laser power value was found that neither contamination nor vibrations in the STEM occur, the few µm wide border region between directly and indirectly heated area is observed. In one carbon grid hole of one specimen at this border, optimal conditions were found and clean enough graphene with implanted nitrogen atoms was observed, see chapter 5. The setup that this sample was produced with is explained in the following paragraph.

At first, the plasma source is turned on with its power supply on $I_{magn} = 16\,\mathrm{mA}$, $U_{an} = 0.05\,\mathrm{kV}$ and $U_{extr} = off$ unplugged. The nitrogen gas line is opened and the target chamber pressure regulated to around $p_t = 3.2 \cdot 10^{-6}$ mbar. Then, the plasma will be ignited, which is visible through the hole in the aperture. The source is supposed to be in this state for around 15-20 minutes to ensure stable operation conditions. After this step, the leak valve is closed again and the sample is laser-cleaned for $t_{cleaning} = 3\,\mathrm{s}$ at a power setting of 6.0 %, which means $P_{cleaning} = 0.27\,\mathrm{W}$. After that, the leak valve is opened again and the target chamber pressure set to $p_t = 3.2 \cdot 10^{-6}$ mbar once more and irradiation starts. The sample that is presented in chapter 5 was irradiated for $t_{irr} = 16\,\mathrm{min}$, while the chamber pressure was between $p_{t,start} = 3.24 \cdot 10^{-6}$ mbar and $p_{t,end} = 3.12 \cdot 10^{-6}$ mbar. Assuming that the ion dose rate as measuerd by the Faraday cup is a good approximation, the total ion dose the specimen was irradiated with was about $N_{sample} = 4.3\,\mathrm{nm}^{-2}$. The laser heated the sample during the entire irradiation time at a power setting of 3.5 %, which is equivalent to $P_{laser} = 0.16\,\mathrm{W}$. All relevant parameters regarding sample preparation are shown in Table 4.10.

Table 4.10: Sample preparation procedure

Step	**Parameters**	**Duration**
1. Degassing	$I_{magn} = 16.0\,\mathrm{mA}$, $U_{an} = 0.05\,\mathrm{kV}$, $U_{extr} = \mathrm{off}$, $p_t = 3.2 \cdot 10^{-6}$ mbar	15-20 min
2. Cleaning	$P_{cleaning} = 0.27\,\mathrm{W}$ (6.0 %)	3 s
3. Irradiation	$P_{laser} = 0.16\,\mathrm{W}$ (3.5 %), $I_{magn} = 16.0\,\mathrm{mA}$, $U_{an} = 0.05\,\mathrm{kV}$, $U_{extr} = \mathrm{off}$, $p_t = 3.2 \cdot 10^{-6}$ mbar	16 min

As pointed out previously, an extraordinary feature of this setup in comparison to others of its kind is the UHV vacuum transfer system between sample preparation area and microscope. Hence after sample irradiation, it can be directly transported into the microscope without exposing it to air. As contamination generally is an issue in experiments involving low-dimensional solids, avoiding specimen-air contact may be a key to limit sample contamination. Because of this UHV vacuum transfer, the samples can be analyzed directly after irradiation takes place without further heating and cleaning steps.

4.2 Analysis

All samples are analyzed using a Nion UltraSTEM 100. This STEM system allows aberration-correction up to fifth order, reaches image resolutions of about 1 Å and, therefore, allows resolving individual carbon atoms. The microscope is operated at a HT of 60 kV to minimize beam damage. A Cold Field Emission Gun (CFEG) with an energy spread of approximately 0.3 eV serves as electron source and the sample chamber pressure typically reaches about 10^{-10} mbar, which is facilitated by a range of $30\,\mathrm{L\,s^{-1}}$ ion pumps along with a $70\,\mathrm{L\,s^{-1}}$ turbo molecular pump for pre-pumping. A description of the standard setup of the UltraSTEM 100 can be found in [42]. In the conducted experiments, the automatic sample exchange and all features related to it remain unused. Instead, a self-constructed manual sample exchange in an UHV environment is used in order to make sample preparation inside the microscope system possible.

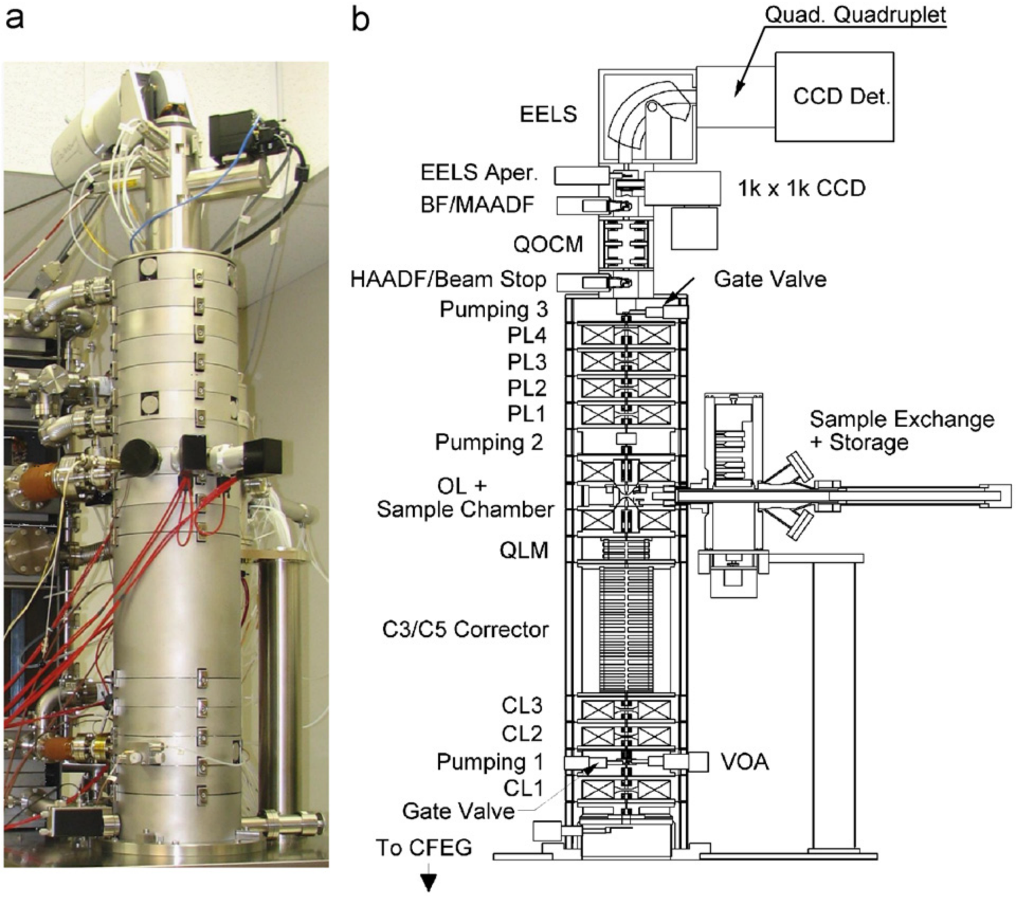
a
b
Quad. Quadruplet
CCD Det.
EELS
EELS Aper.
1k x 1k CCD
BF/MAADF
QOCM
HAADF/Beam Stop
Gate Valve
Pumping 3
PL4
PL3
PL2
PL1
Sample Exchange
+ Storage
Pumping 2
OL +
Sample Chamber
QLM
C3/C5 Corrector
CL3
CL2
Pumping 1
VOA
CL1
Gate Valve
To CFEG

Figure 4.1: (a) Photo and (b) model of Nion UltraSTEM 100 [42]

Figure 4.1 shows a photo and model image of the column of the STEM. It has three condenser lenses (CL) that enable tuning of source demagnification and beam current independently. The objective lens (OL) is a symmetric, Riecke-Rusky type condenser-OL that is optimized for low chromatic aberration with $C_c \approx C_s \approx 1\,\mathrm{mm}$. Between CLs and OL, the third-generation Nion C3/C5 corrector nullifies third and fifth order aberrations. It consists of 12 rotatable quadrupoles and three combined quadrupole-octopoles. Due to the high complexity and the degrees of freedom of the aberration correction system, a software that iteratively optimizes the aberration coefficients is available. The quadrupole lens module (QLM) electron-optically couples the corrector to the OL. The projection system consists of four lenses (PL), particularly useful for recording diffraction patterns. Changing any lens settings does not have an impact on their heat output, as they are supplied by two independent power supplies keeping power dissipation constant.

The newly designed sample stage exhibits a high stability and limits sample drift. Due to its construction, when the stage is heated up uniformly, to the first order, there is no change of the sample position. This friction-free stage design may be vulnerable to vibrations, though. That is particularly important, as in the present setup a vacuum line leading from the sample preparation area to the microscope may easily couple vibrations. To minimize them, vibration dampers are installed at the lightweight and stiff stage. Besides high stability, the stage is highly precise, allowing it to get close to the sample's optimal defocus value mechanically. The fine tuning of defocus is achieved by adjusting the HT.

The UltraSTEM 100 has a range of detectors, including CCD, MAADF, HAADF and EELS. For tuning and orientation on the sample, the CCD camera is utilized. The MAADF detector covers semi-angles from 40 to 60 mrad, while EELS detects electrons between 0 and 60 mrad. This means that if MAADF and EELS are used at the same time, the EELS signal intensity suffers. Therefore, MAADF is only utilized when EELS is not required. At all other times, HAADF and EELS are employed simultaneously. In case of the HAADF image contrast difference between carbon and nitrogen being too small, EELS enables elemental identification of single atoms, while the HAADF detector gives an image of the observed structure. In this way, atomically resolved images of configurations of nitrogen atoms that are reliably identified as such are observed. Furthermore, this setup enables the creation of spectrum images that contain an EEL spectrum in every pixel of the corresponding HAADF image. The energy resolution of the EELS measurements is about 1 eV, which is sufficient to measure the nitrogen peak at around 400 eV [43].

The analysis software used in the experiments, Nion Swift, is provided along with the microscope. A hardware PC has direct access to the microscope and a user PC runs Swift that offers simplified controls such as point and click shifting of the sample and the saving of locations on the sample as well as all controls necessary for the measurement. This includes detector settings, HAADF, EELS and spectrum image parameters, CCD camera management, the aberration tuning algorithm, electron source and aperture controls and others. All data is recorded using Swift.

Chapter 5

Results and Discussion

5.1 Overview

With the setup described in section 4.1, it was possible to produce a sample with large clean spots with various nitrogen doping sites and, as a result of the high ion dose that was applied, a high defect density. Figure 5.1 is a MAADF image of a typical clean spot on the sample at atomic resolution. The high defect and silicon densities that can be seen were observed at other spots as well. Images with a larger field of view (FOV) that display the extent of contamination are found in Figures A1 and A2 in Appendix. Most images presented in this chapter have an optical resolution of about 1 Å.

Contrary to the findings in [35], MAADF image contrast difference between carbon and nitrogen atoms was not sufficient to identify nitrogen atoms reliably. A few nitrogen atoms could be found through their MAADF contrast during the experiments, however, carbon atom contrast variations were large enough to reach a similar contrast difference. Therefore, no reliable identification of nitrogen atoms solely through MAADF imaging is possible with the present setup. HAADF image contrast differences are larger, however, due to the higher detection angles, the signal intensity is lower leading to the same problem. As a consequence, all nitrogen atoms were identified by single-atom EELS. Doping densities could not be determined through EELS over large areas, as the signal-to-background ratio of the nitrogen peak is too low. The results presented in this chapter, therefore, consist of HAADF images and their corresponding EEL spectra and a few spectrum images, as far as sample drift allowed it. They are sorted by the kind of nitrogen configuration that is found, namely graphitic, pyridinic, pyrrolic. Besides single HAADF images with their respective EEL spectra, there are image series at the same spot, also usually limited by sample drift. The time between series images is generally in the range of 20 s to 3 min. Since the nitrogen configurations that were observed are dynamic under the electron beam, image series may include different configurations. They will be presented in the subsection about the configuration that is observed first. It must also be noted that in series of images, single atoms cannot be tracked. Hence a nitrogen atom close to the location of one in the image before may as well be a second atom that is not the one identified as such in the first image. Also, single-atom

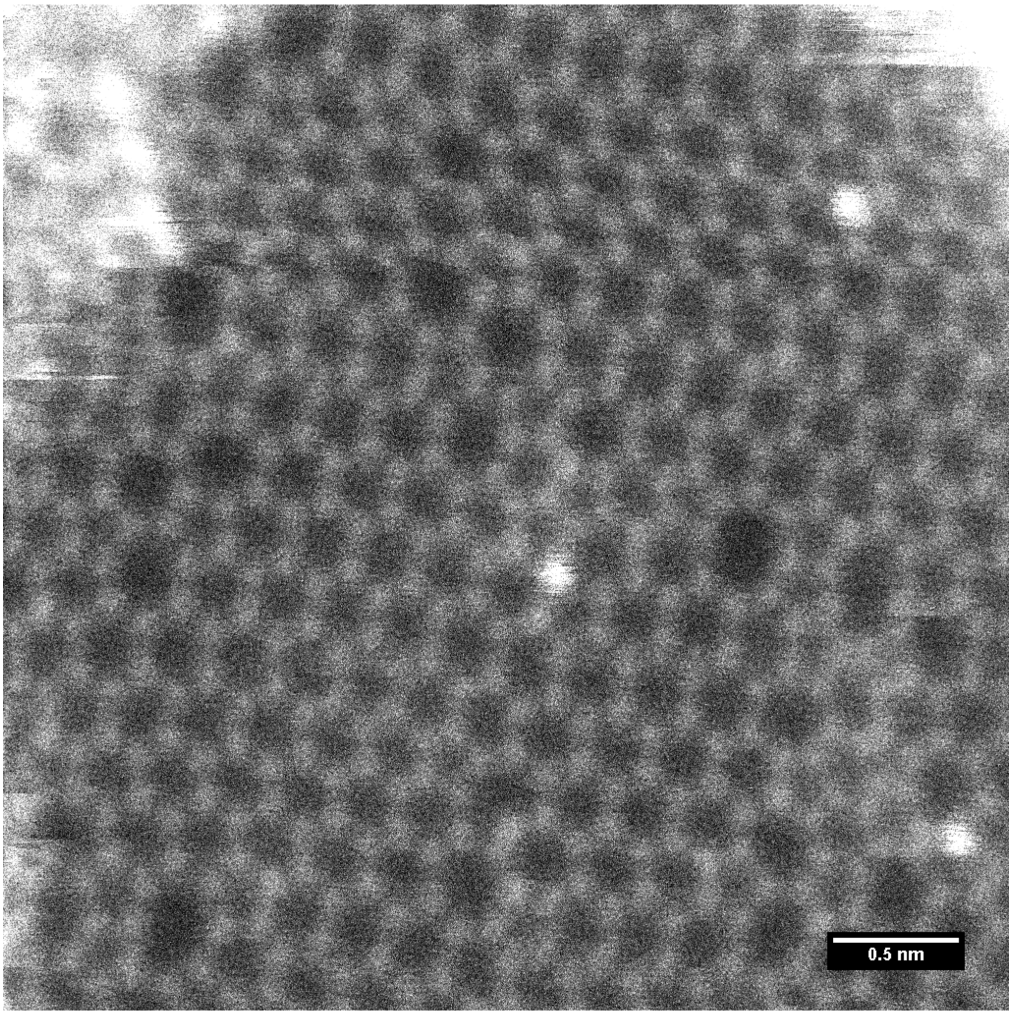

Figure 5.1: Representative MAADF image at clean spot

EELS only allows the identification of one nitrogen atom at a time, except for spectrum images. The HAADF image contrast suggests where further nitrogen atoms may be located, though. Furthermore, a spectrum image with many doping sites is presented in section 5.3. The HAADF images presented in this chapter show the region of interest from the original image and are filtered by a Gaussian filter. Corresponding atomic EEL spectra, including the background-subtracted graphs, are shown to confirm the presence or absence of nitrogen. The background was fitted by $A \cdot \Delta E^{-B}$ in a window just before the nitrogen edge.

5.2 Nitrogen Configurations

5.2.1 Pyrrolic

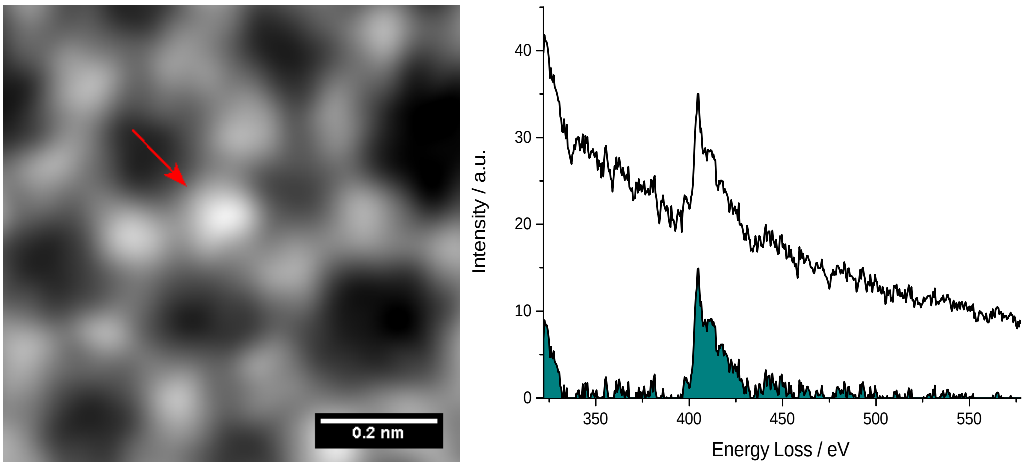

(a) Filtered HAADF image (b) Single-atom EEL spectrum

Figure 5.2: Pyrrolic nitrogen doping site 1

Descriptions of the three relevant nitrogen configurations, namely graphitic, pyridinic and pyrrolic, are given in section 3.1. Figure 3.1 illustrates them and, as can be seen, pyrrolic nitrogen is the name given to nitrogen doping sites where the nitrogen is part of a pentagon. It is expected to be the least stable configuration among the three. A first example of pyrrolic nitrogen is presented in Figure 5.2. Figure 5.2a depicts a section of the originally recorded HAADF image, which is found in the appendix, Figure A3. The atomic EEL spectrum at the center of this section can be seen in Figure 5.2b.

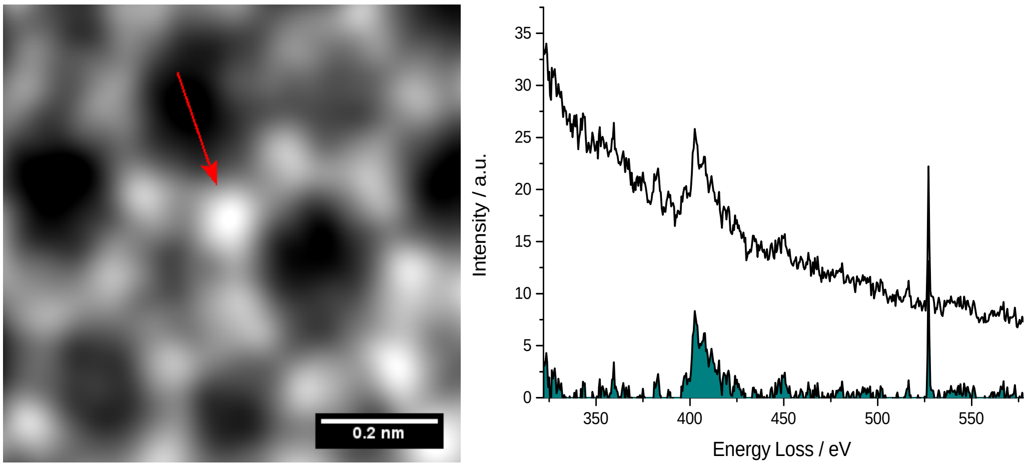

(a) Filtered HAADF image (b) Single-atom EEL spectrum

Figure 5.3: Pyrrolic nitrogen doping site 2

The presence of the nitrogen atom is indicated by its HAADF image contrast and confirmed by the EEL spectrum. A significant nitrogen peak with its edge close to 400 eV is observed. The nitrogen atom is part of two hexagons and one pentagon (5-6-6), making it a pyrrolic structure that is similar to graphitic nitrogen. Unlike the model of a pyrrolic nitrogen site in Figure 3.1, the nitrogen atom is not part of a heptagon. However, the pentagon that it is part of neighbours two heptagons.

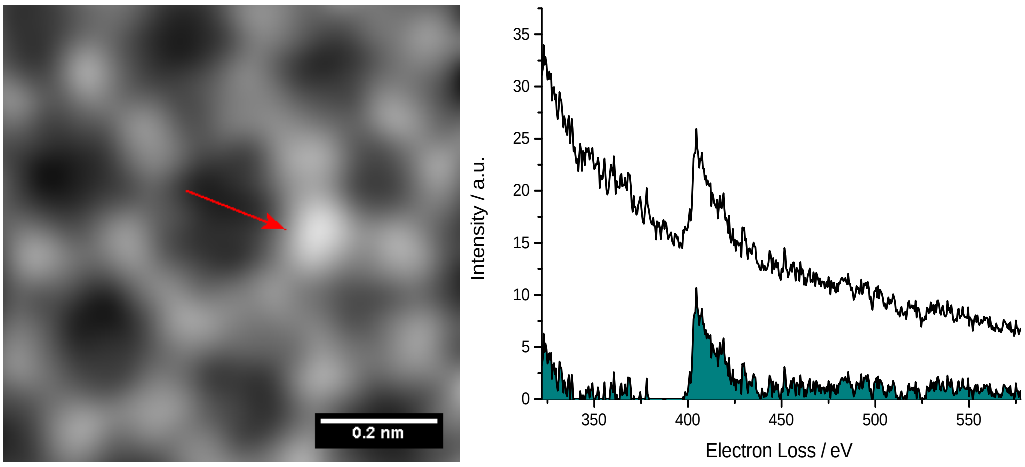

(a) Filtered HAADF image

(b) Single-atom EEL spectrum

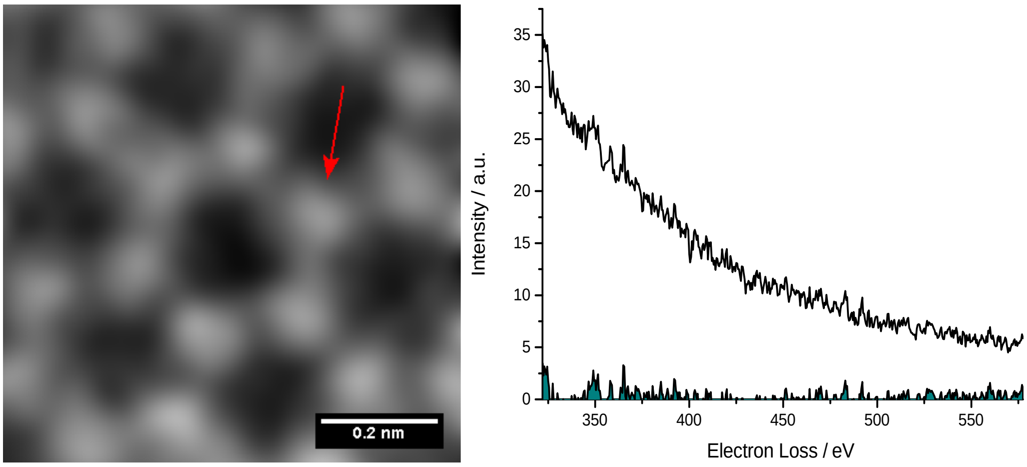

(c) Filtered HAADF image

(d) Single-atom EEL spectrum

Figure 5.4: Pyrrolic nitrogen doping site 3

A similar doping site is shown in Figure 5.3. This site is at a different location on the sample. The complete image is shown in the appendix, Figure A4. The nitrogen atom is part of a pentagon and two septagons. Therefore, the lattice is the same as in Figure 5.2, just the position of the nitrogen is different.

A series of two images of a pyrrolic nitrogen doping site is presented in Figure 5.4. As can be seen in Figure 5.4a, a third configuration of pyrrolic nitrogen was observed. In this one, the N atom is part of two pentagons and one heptagon. This proves the existence of three of six possible combinations regarding pyrrolic nitrogen doping sites, only considering pentagons, hexagons and heptagons. These are the nitrogen being part of a pentagon and two hexagons (5-6-6), being inside a pentagon and two heptagons (5-7-7) and two pentagons and a heptagon (5-5-7). The other three configurations are 5-5-5, 5-5-6 and 5-6-7. A further investigation on these configuration subtypes is found in subsection 5.2.4.

The subsequent image at the same position displayed in Figure 5.4c and the corresponding EEL spectrum in Figure 5.4d show that, under the influence of the electron beam, the defect configuration changed and the nitrogen diffused. This indicates the low stability of pyrrolic species that is expected, as described in section 3.2. See Figures A5 and A6 for the full images corresponding to Figure 5.4.

5.2.2 Pyridinic

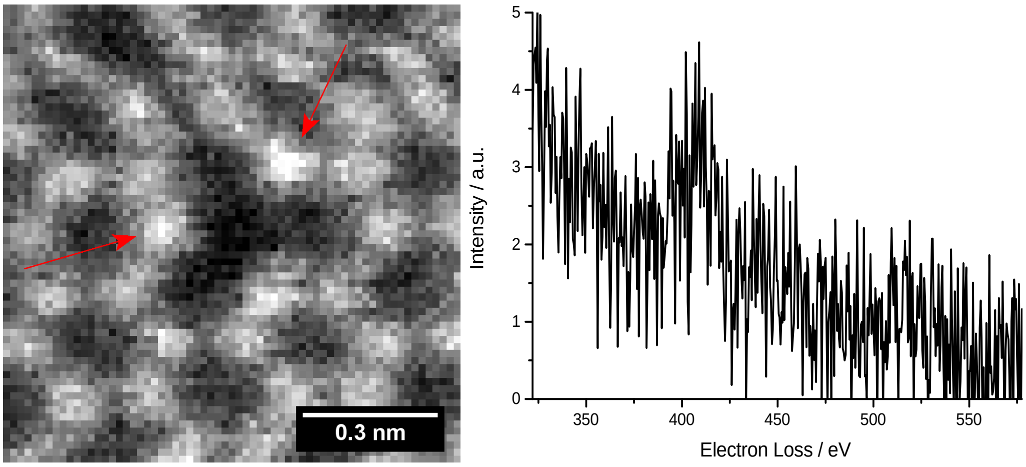

(a) Spectrum image HAADF image

(b) Summed EEL spectrum

Figure 5.5: Pyridinic nitrogen doping site 1

By far less often observed than pyrrolic nitrogen were pyridinic doping structures. As this means nitrogen that has two C-N bonds in a hexagon and no third bond, a neighboring vacancy is required. Figure 5.5 presents a spectrum image of a single vacancy next to two pyridinic nitrogen atoms, including the HAADF image recorded during the spectrum image acquisition in Figure 5.5a and the sum of the spectra of pixels around both marked nitrogen atoms in Figure 5.5b. As the time for EEL spectrum acquisition of single atoms in spectrum images is small in comparison to single-atomic EELS, the SNR is low. Nonetheless, a peak at a slightly higher energy than 400 eV is clearly visible. This is valid for both individual EEL spectra. However, the third corresponding atom neighboring the single vacancy does not show a nitrogen peak in its EEL spectrum. Even though the HAADF image contrast may suggest that this is a third nitrogen atom in this configuration, the EEL measurement identifies it as a carbon atom. The mean contrast values of circular areas around the atomic centers with a diameter of 5 pixels are 0.0258 (N), 0.0243 (N) and 0.0233 (C) compared to 0.0221 of a nearby carbon atom with a high image contrast compared to other carbon atoms around. This emphasizes the necessity of utilizing EELS in order to doubtlessly distinguish carbon and nitrogen atoms. The atomic configuration in Figure 5.5 has been observed in [28] as well and can be seen in Figure 3.6d. The entire HAADF image corresponding to the spectrum image is attached as Figure A7.

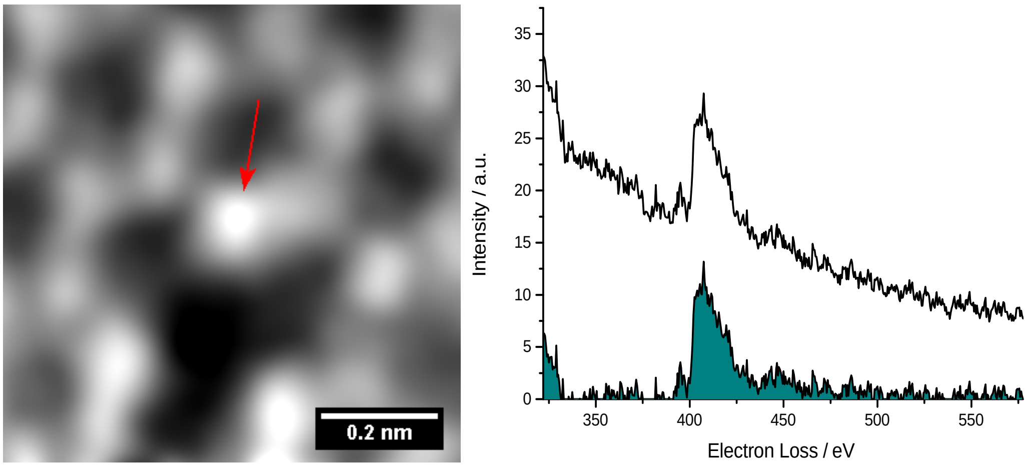

(a) Filtered HAADF image (b) Single-atom EEL spectrum

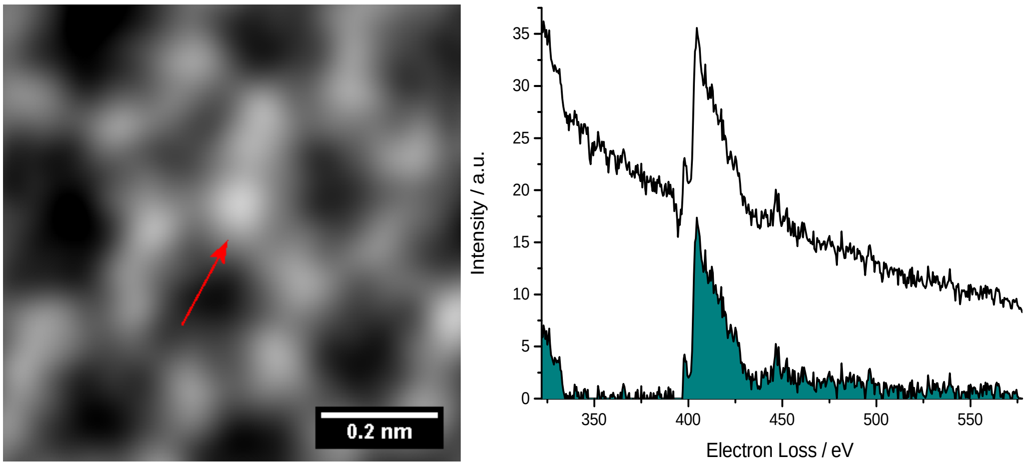

(c) Filtered HAADF image (d) Single-atom EEL spectrum

Figure 5.6: Pyridinic nitrogen doping site 2

A dynamic view on a pyridinic nitrogen doping site is offered by Figure 5.6. The configuration is similar to the previous one in Figure 5.5. HAADF image contrast suggests that three nitrogen atoms are part of this structure, however, as these are images where single-atomic EELS was utilized, only the atom in the center of Figure 5.6a can be verified to be a nitrogen atom. That at least two nitrogen atoms are part of this defect is reasonable, though, because single pyridinic nitrogen tends to form structures similar to Figure 3.6b and c. Figure 5.6c shows a subsequent image at the same location. The EEL spectrum in Figure 5.6d confirms that there is still a nitrogen atom present at this spot. However, the configuration around it transformed from pyridinic to 5-6-6 pyrrolic.

Furthermore, Figure 5.6b illustrates that the nitrogen EELS peak's fine-structure allows the identification of pyridinic nitrogen, as predicted in [28]. A small peak between 390 and 400 eV is visible. For pyrrolic and graphitic nitrogen, this peak is not observed, see sections 5.2.1 and 5.2.3.

5.2.3 Graphitic

The most simple process to have a nitrogen ion from the plasma source directly implanted into the SLG lattice is perfect substitution. If one carbon atom is ejected by a nitrogen ion and it takes up the position of the carbon atom, the resulting species is graphitic nitrogen. However, other processes may also lead to this configuration, e.g. lattice rearrangements caused by external influence, transforming pyrrolic nitrogen into graphitic nitrogen. Trapping of nitrogen atoms in single vacancies may lead to graphitic N as well.

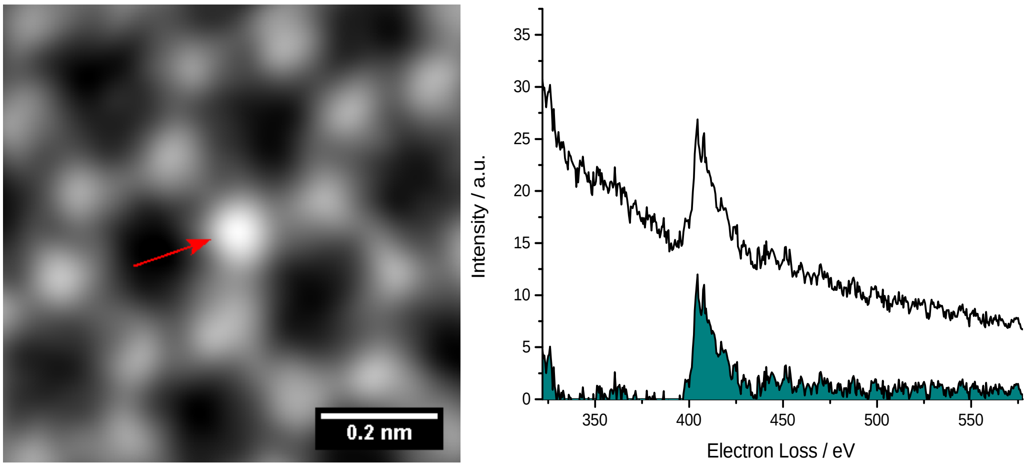

(a) Filtered HAADF image (b) Single-atom EEL spectrum

Figure 5.7: Graphitic nitrogen doping site 1

A perfect graphitic nitrogen doping site that is similar to Figure 3.6a can be seen in Figure 5.7. The HAADF image contrast and EEL spectrum of the central atom confirm that it is nitrogen. The entire image can be found in the appendix, Figure A10.

Three graphitic nitrogen doping sites are presented in a spectrum image in Figure 5.8a. The corresponding EEL spectra confirm this, the sum of all three is shown in Figure 5.8b. All three nitrogen atoms are part of three hexagons each (6-6-6), while two are in the same and the third is in a neighboring hexagon. This opposes observations that were made in [28]. There, it is stated that "the concentration of graphitic-N do[p]ing in graphene has never exceeded a few atom % because the N@C [= graphitic nitrogen] atoms cannot come closer to each other. Multiple graphitic-N atoms have never been found to coexist in a hexagonal unit of graphene. The shortest distance between two graphitic-Ns we found is 6.2 Å in our N-doped graphene". Figure 5.8 proves that configurations with two graphitic nitrogen defects at a distance of around 2.3 Å do exist. Hence high doping

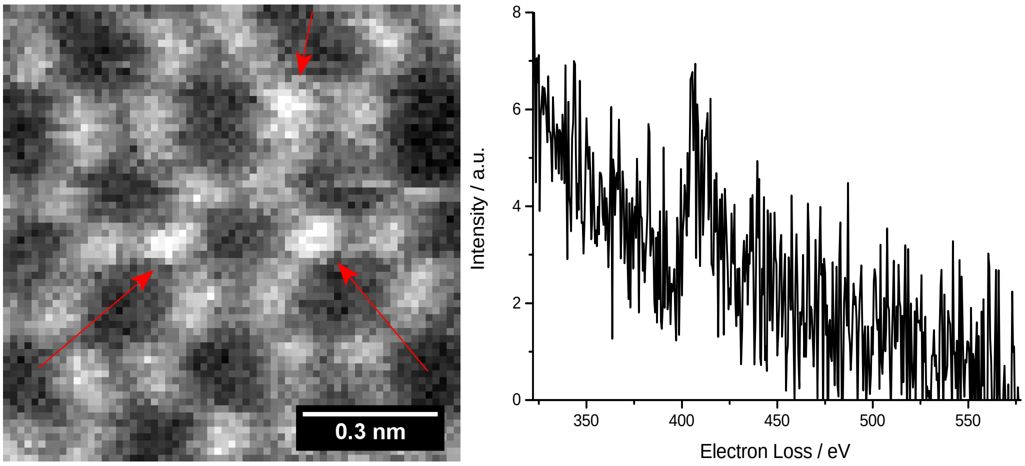

(a) Spectrum Image HAADF image

(b) Summed EEL spectrum

Figure 5.8: Graphitic nitrogen doping site 2

densities through graphitic nitrogen are feasible. So far, only doping configurations with the nitrogen atom being part of three hexagons have been presented, however, there may be structures where it is part of two hexagons and one heptagon as well. This can be seen in Figure 5.9a.

Figures 5.9b, 5.9d and 5.9f illustrate the EEL spectrum of the central atom in each corresponding HAADF image. As a distinct peak can be seen in all three EEL spectra, Figures 5.9a, 5.9c and 5.9e all show nitrogen doping structures. The kind of structure changed during observation as a consequence of the electron irradiation. The original structure was a graphitic 6-6-7 configuration, it transformed into a 5-6-6 pyrrolic nitrogen doping site and, eventually, into 6-6-6 graphitic N. This shows that even a 6-6-7 graphitic structure is unstable under the electron beam. During the experiments, no transformation of a 6-6-6 graphitic nitrogen structure was observed.

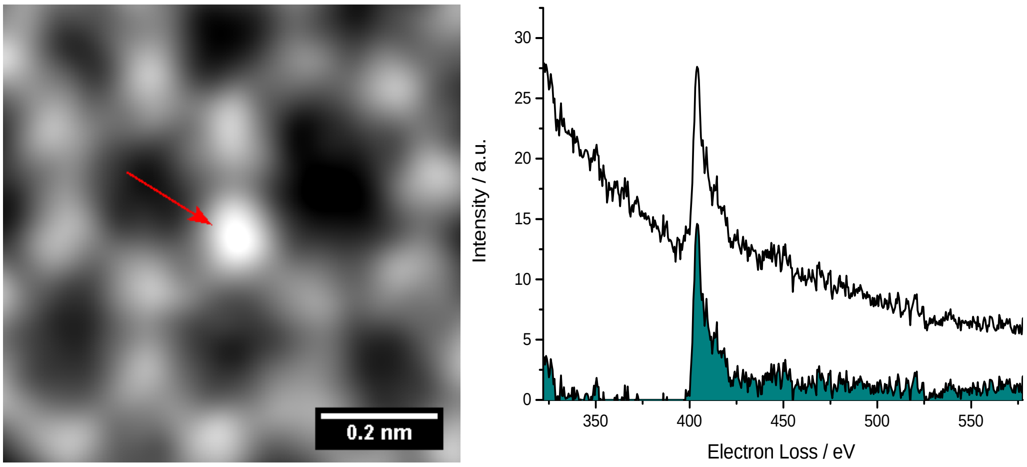

(a) Filtered HAADF image (b) Single-atom EEL spectrum

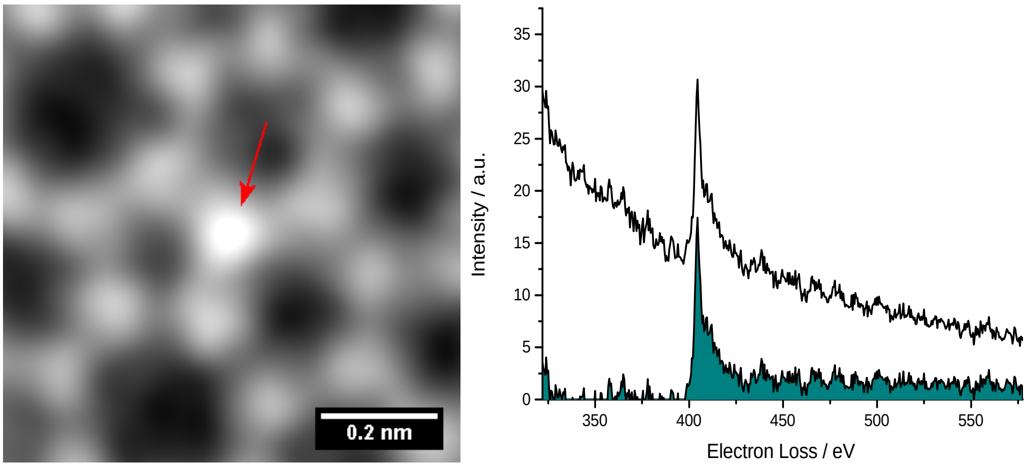

(c) Filtered HAADF image (d) Single-atom EEL spectrum

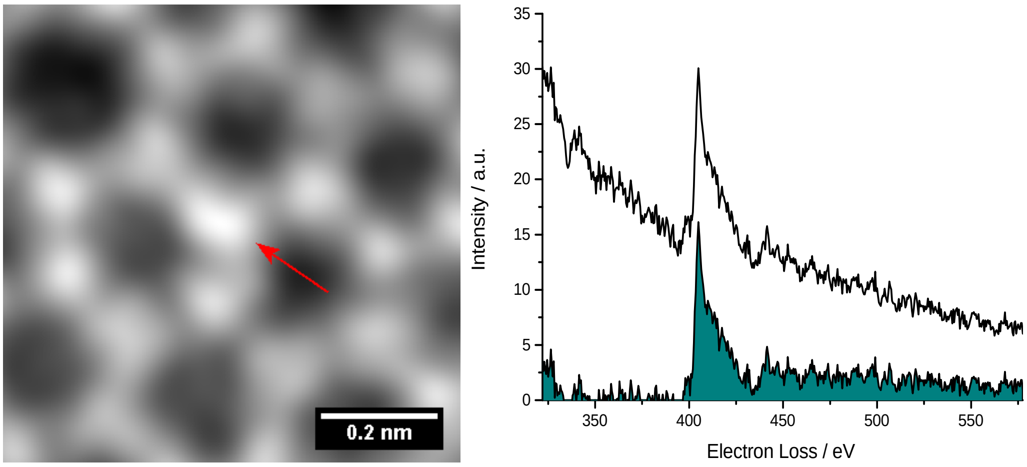

(e) Filtered HAADF image (f) Single-atom EEL spectrum

Figure 5.9: Graphitic nitrogen doping site 3

5.2.4 Distribution of Nitrogen Species

Graphitic nitrogen is the most stable doping species [27] and the most probable one to be the result of the present ion irradiation [13]. However, this does not take the laser heating of the sample and the effect of the electron irradiation during the imaging process of about $2 \cdot 10^8\ \mathrm{s}^{-1}$ ($= 25\,\mathrm{pA}$) into account. To allow a comparison of the results from the experiments with other studies, specifically to those mentioned in section 3, this section presents the distribution of nitrogen species among all analyzable images acquired in this work. This means single images, images series and spectrum images. All atoms that were identified through EELS are counted. Series are counted in a way that an unchanged configuration in two different images is counted only once. If the species changed, both, before and after the transformation, are calculated. In spectrum images, all atoms that could be identified are summed up. A change from one substructure[3] to another, e.g. 5-5-6 pyrrolic to 5-6-6 pyrrolic, is counted as both substructures, but only once as pyrrolic. One pyridinic and four pyrrolic substructures cannot be definitely identified and are omitted, so only the species, i.e. pyrrolic, pyridinic or graphitic, is counted. Altogether, 53 nitrogen doping sites were categorized. They are identified to be either graphitic, pyridinic or pyrrolic nitrogen. Graphitic nitrogen structures are divided into 6-6-6, 6-6-7 and 6-6-8 configurations, while pyrrolic N is classified into 5-5-6, 5-5-7, 5-6-6, 5-6-7 and 5-7-7 structures. Pyridinic nitrogen doping sites are sorted by the amount of nitrogen atoms. Pyridinic nitrogen sites with one (1N+SV), two (2N+SV) and three (3N+SV) have all been observed. The structures are equivalent to those seen in Figure 3.6. While it is expected that pyridinic nitrogen in a configuration of this kind may also be in a heptagon, only such were observed that are part of a hexagon. Table 5.1 and Figure 5.10 illustrate the distribution of nitrogen species found in the experiments. About one out of two observed nitrogen doping sites were pyrrolic N. With 42%, slightly less doping structures were graphitic and the remaining small fraction, nearly one out of ten, was pyridinic nitrogen. This includes only atoms that were confirmed to be nitrogen through EELS measurement. This means that in spectrum images all nitrogen atoms are counted, while for single-atomic EELS, only one is counted. The quantity of pyridinic nitrogen substructures refers only to those atoms that were identified to be nitrogen by EELS. However, for the identification of the substructure, the HAADF image contrast values have been considered for unidentified atoms.

The fact that pyrrolic N sites are more common than graphitic ones indicates that there are mechanisms to create pyrrolic nitrogen directly by ion irradiation. The creation of pyrrolic nitrogen requires either the transformation of another species into pyrrolic N by the electron beam or the presence of defects, which may allow the nitrogen ions to be implanted as pyrrolic species directly. However, as graphitic N is expected to be more stable under the electron beam than pyrrolic nitrogen, the influence of the electron beam would tend to increase the share of graphitic and lower the share of pyrrolic nitrogen. Hence the high share of pyrrolic nitrogen indicates the presence of interactions of incident nitrogen ions with defected graphene that directly lead to pyrrolic N. If these deductions are true, it is expected that such interactions with defected graphene are more likely to occur than perfect substitution as an interaction with pristine graphene. This is due to the small share of defected graphene in comparison to pristine graphene spots and the ratio of pyrrolic to graphitic nitrogen, nonetheless, being about 1:1. In [13], pristine graphene is simulated, which does not take into account that many defects are created during irradiation. The high defect density of the graphene in this work can be seen in Figure 5.1. It has not been measured directly, but was observed consistently throughout the experiments. In [35], it is stated that defects that were created by ion irradiation can be filled with nitrogen, allowing higher substitution-to-defect ratios. This may be a description of the above described effect that is responsible for the high share of pyrrolic nitrogen.

---

[3] species refers to graphitic, pyrrolic and pyridinic nitrogen, while structure/substructure mean the specific configuration around the nitrogen atom, e.g. 6-6-6 graphitic nitrogen

Table 5.1: Distribution of nitrogen species

Species	**Amount observed**	**Structure**	**Quantity**
Graphitic	22	6-6-6	19
		6-6-7	2
		6-6-8	1
Pyridinic	5	1N+SV	1
		2N+SV	1
		3N+SV	1
Pyrrolic	26	5-5-6	2
		5-5-7	1
		5-6-6	11
		5-6-7	7
		5-7-7	2

During the experiments, the transformation of 6-6-7 graphitic nitrogen into pyrrolic N was observed, not from 6-6-6 graphitic to pyrrolic. However, pyrrolic nitrogen structures transforming into 6-6-6 graphitic were observed. This allows only two explanations - either transformations of 6-6-6 graphitic N to pyrrolic nitrogen regularly take place and have just not been observed or the irradiation times and corresponding electron doses are clearly smaller than necessary to make the sample reach its preferred configuration, namely graphitic nitrogen. In all other cases, the vast majority of doping sites must be graphitic. A further investigation on the effect of electron irradiation on this SLG sample can be found in section 5.3.

Regarding pyridinic nitrogen, three kinds of structures have been observed. In Table 5.1, they are called 1N+SV, 2N+SV and 3N+SV, as they include one, two and three nitrogen atoms, respectively. One of four pyridinic nitrogen configurations that were observed could not be classified, but is likely to be either a 2N+SV or 3N+SV struc-

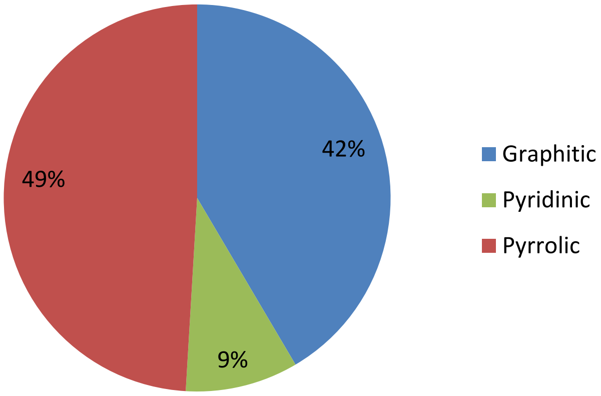

(a) Distribution of nitrogen species

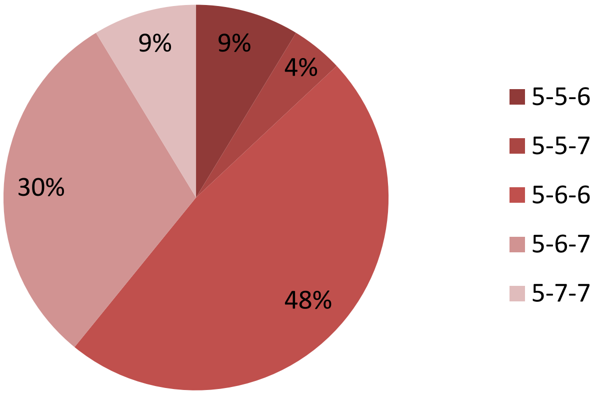

(b) Distribution of pyrrolic N structures

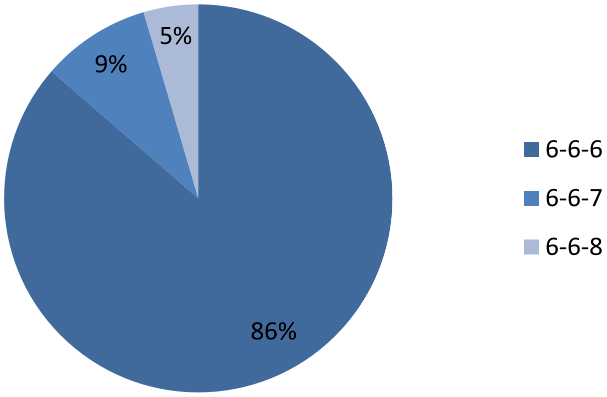

(c) Distribution of graphitic N structures

Figure 5.10: Distribution of Nitrogen Species

ture. These structures conform with those shown in Figure 3.6b/c (1N+SV), d (2N+SV) and e (3N+SV). In [28], only large shares ($\approx 30 - 35\%$) of pyridinic N are observed. Also, in [31], small shares of pyridinic nitrogen are only observed for bi-layer graphene samples. For SLG, similar shares of pyridinic N as in [28] were observed. Figure 5.10a shows that in this examination only 9% of confirmed nitrogen atoms were in a pyridinic configuration. As single-atomic EELS is only able to identify one nitrogen atom in a pyridinic structure, those that are likely to be nitrogen based on their HAADF contrast could be considered as well. This would increase the percentage of pyridinic nitrogen to $\approx 14\%$, which is still low. Generally, a low share is expected, as carbon adatoms on the graphene surface may fill pyridinic doping sites, leading to graphitic N. The discrepancy to the other experimental results may be explained by a low stability under the electron beam of pyridinic configurations or the effect of constant laser heating.

Three kinds of graphitic nitrogen were observed. These are, a nitrogen atom that replaced one carbon atom in the graphene lattice without further disturbance (6-6-6 graphitic N), a similar configuration with the nitrogen atom being part of a heptagon (6-6-7) and a third, where it is in an octagon (6-6-8). 6-6-7 and 6-6-8 are far less common than 6-6-6, which suggests a higher stability of the 6-6-6 arrangement.

As explained in subsection 5.2.1, there are six different substructures of pyrrolic N, only considering pentagons, hexagons and heptagons. Five of these possible configurations were observed at least once. 5-6-6 has been observed most often with nearly one out of two cases and 5-6-7 at around 30 %, 5-5-6 and 5-7-7 were uncommon and 5-5-7 only detected once. This means that structures with more of the original graphene's hexagons around the nitrogen atom and a cross sum, in the given nomenclature, closer to 18 occur more regularly than others. The hexagon-condition supposedly is related to transformation probabilities. A structure with more original hexagons requires less transformations to take place and hence is easier and more probable to be created. The cross-sum-condition may be related to the stability of a structure under the electron as well as threshold energies that need to be overcome to transform into less stable configurations and, therefore, transformation probabilities.

5.3 Large Field-of-View Spectrum Image

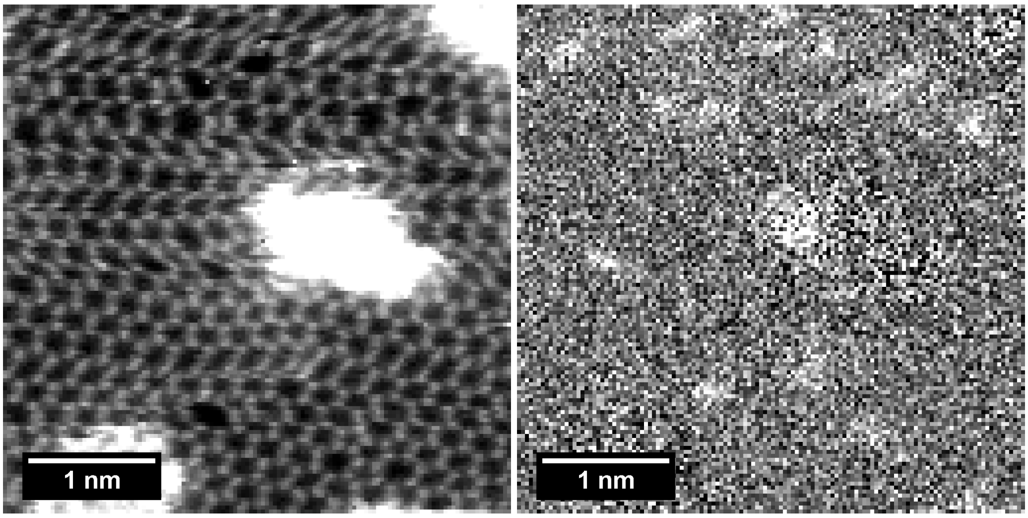

(a) HAADF image (b) Energy filtered spatial EEL intensity

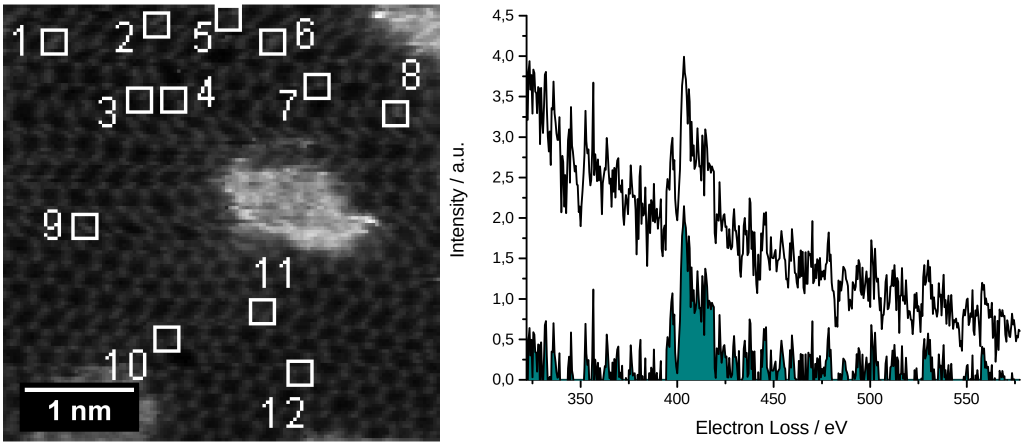

(c) N atom locations (d) EEL spectrum of N atom 8

Figure 5.11: Large area spectrum image

During the experiments, sample drift strongly limited the extent to which spectrum images could be acquired. Nonetheless, one spectrum image over an area of 4x4 nm was measured. Figure 5.11 shows the simultaneously acquired HAADF image (5.11a), the energy filtered image (5.11b), all confirmed doping sites (5.11c) and a representative EEL spectrum (5.11d). The image in Figure 5.11b was created by only taking electrons with energy losses between 397 eV and 421 eV into account.
As indicated in Figure 5.11c, on the 16 nm^2 FOV, there are $N_N = 12$ nitrogen atoms in the SLG lattice. Most of them can be found when searching for high intensities in Figure 5.11b. However, as it is most reliable, the summed EEL spectra of the surrounding area of every suspected nitrogen atom were evaluated, as before. The distinctiveness of all 12 peaks is similar to the spectrum seen in Figure 5.11d. Initially, it was expected that

utilizing EELS will allow a quantification of the nitrogen doping density. For EELS over larger areas, the signal-to-background ratio, i.e. the nitrogen peak size in comparison to the carbon background, was too low in order to confirm the existence of nitrogen in the sample lattice or evaluate the doping density over large areas. Therefore, the best quantification of the doping density in this investigation is achieved through this 16 nm^2 spectrum image. N_N is the amount of nitrogen atoms in the spectrum image, A_C is half of the unit cell area of graphene and A_{FOV} is the Field of View (FOV). The doping density is calculated as shown in equation (5.1).

$$N_{doping,\%} = \frac{N_N \cdot A_C}{A_{FOV}} \tag{5.1}$$

For $N_N = 12$, $A_C = 0.026\,\mathrm{nm}^2$ and $A_{FOV} = 16\,\mathrm{nm}^2$, equation (5.1) results in

$$\boxed{N_{doping,\%} = 2.0 \text{ at.\%}}$$

A doping density of 2.0 at.% is high compared to similar studies. In [35], a doping density of 1 at.% is reported and in [29] 1.6 at.% for bilayer graphene on a substrate. However, as the doping density of the present sample is evaluated only based on a measurement in an area of 16 nm^2, it is uncertain. The location of the spectrum image on the sample was not chosen because of its high defect density. It was the only one over a wider area that the experimental conditions allowed to be acquired. Therefore, the pick of this region on the sample can be considered random. Furthermore, part of the spectrum image in Figure 5.11 is covered by contamination, which also contains nitrogen atoms. Hence the doping density in this area is actually larger than the stated 2.0 at.%. In section 4.1, the ion dose per area N_{sample} was determined using a Faraday cup. The result was $N_{sample} = 4.3\,\mathrm{nm}^{-2}$. Expressed in the same units as the ion dose, the doping density is $N_{doping} = 0.75\,\mathrm{nm}^{-2}$, which means that the ratio of doping density to ion dose is around 17%. Hence the amount of doping atoms is lower by less than an order of magnitude than the incident ion dose. Simulations predicted a maximum probability of 58% [13]. Considering that the acceleration voltage in the present setup may be not exactly at its optimum, that saturation effects could become relevant when applying high doses and that the predictions of a theoretical model do not necessarily give a good approximation for a specific experiment, a ratio of 17% is reasonable. Other studies have shown similar results in this regard [35]. Besides the amount of nitrogen atoms in this 16 nm^2 spectrum image, the doping structure of each of the 12 sites is investigated. Table 5.2 shows the outcome.

Table 5.2: Species and Structures of Nitrogen Atoms in Figure 5.11

Nitrogen Atom	**Species**	**Structure**
1	pyrrolic	5-6-6
2	graphitic	6-6-6
3	pyrrolic	5-6-6
4	pyrrolic	5-6-7
5	pyrrolic	5-6-6
6	pyrrolic	5-6-6
7	pyrrolic	5-6-7
8	graphitic	6-6-6
9	graphitic	6-6-6
10	graphitic	6-6-8
11	pyrrolic	5-6-7
12	pyrrolic	5-6-6

Chapter 6

Conclusion and Outlook

6.1 Conclusion

Nitrogen has been successfully implanted into SLG using a low-energy ion plasma source. This method has been proposed as an alternative to chemical processes that suffer from contamination [29]. As this investigation has shown, low-energy ion treatment of suspended SLG leads to heavy contamination as well. This made continuous laser heating of the sample necessary during ion irradiation. Furthermore, HAADF and MAADF image contrast did not allow clear identification of nitrogen atoms. It is sufficient to suggest which atoms may be nitrogen, though. Single-atom EELS was utilized for the definite identification of single atoms. EELS over large areas did not yield sufficient signal strengths to calculate doping concentrations. A large area spectrum image permitted the best approximation of the doping concentration of around 2 at.%. This is the same order of magnitude as the expected impact of the applied ion dose that corresponds to 7 at.%. The plasma treatment leads to a high defect density of the same order of magnitude as well. During the experiments, a low reproducibility has been observed. The same parameters governing the plasma consistently lead to different results regarding the sample. This makes assured conclusions in research problematic and may hinder reliable industrial production. Therefore, arbitrariness could constitute a serious obstacle of plasma treatment being utilized in graphene doping. If the vacuum transfer system between sample preparation area and microscope, that was present in the experiments, is necessary, or at least benefiting, could not be found out. Contamination generally was too arbitrary as well.

Graphitic, pyridinic and pyrrolic nitrogen doping sites were observed and exemplary images presented in this study. Pyrrolic and graphitic nitrogen were most numerous with 51 % and 40 %, respectively. Only 9 % of atoms that were confirmed to be nitrogen by EELS measurement were pyridinic. This shows that low-energy plasma treatment leads to the creation of all three kinds of nitrogen doping in significant numbers. The results differ from those published in [27], where mostly graphitic doping was observed, while pyridinic N was common and pyrrolic N rare. However, there, the nitrogen ion energy was 1 kV. Regarding graphitic nitrogen doping sites, three different kinds were found.

Firstly, 6-6-6 graphitic nitrogen that refers to a dopant atom that simply replaced one carbon atom and, therefore, is part of three hexagons. Secondly, 6-6-7 graphitic N that is also part of a heptagon and thirdly, 6-6-8 with an octagon instead of the heptagon. The probability to find one of these graphitic structures was found to depend directly on how similar it is to pristine graphene. Furthermore, it was shown that strict limits regarding the achievable doping density through graphitic nitrogen postulated in [28] are not existent. The observations that were made for pyrrolic nitrogen are similar to those of graphitic N. Only pyrrolic nitrogen with three C-N bonds were detected. Neglecting octagons and larger carbon rings, there are six possible configurations of pyrrolic three-bond nitrogen. Except for 5-5-5 pyrrolic nitrogen, all these structures have been observed, namely 5-5-6, 5-5-7, 5-6-6, 5-6-7 and 5-7-7 pyrrolic nitrogen. The more hexagons there were in a configuration and the closer the cross sum in the given nomenclature was to 18, the more frequent it was. Hence 5-6-6 was the most common pyrrolic nitrogen doping site followed by 5-6-7. Three different kinds of pyridinic nitrogen have been observed, namely consisting of a single vacancy and one (1N+SV), two (2N+SV) and three (3N+SV) nitrogen atoms, respectively. They conform with the structures presented in [28].

No reliable statements about the stability of all of these nitrogen doping structures can be made. However, a series of transformations between them was observed, as many or all of them are not stable under the 60 kV electron beam of the STEM. Transformations that were observed include pyrrolic to graphitic and pyridinic to pyrrolic as well as graphitic to pyrrolic nitrogen. This shows that under exposure of electron irradiation all observed doping species can translate into each other. However, no transformation of a 6-6-6 graphitic structure was detected, even though this configuration occured frequently. A transformation into pyridinic nitrogen has not been observed as well. The data suggests that the high percentage of pyrrolic nitrogen is caused by the electron irradiation. Moreover, it was shown that the EELS peak fine-structure allows the identification of pyridinic nitrogen, confirming observations from [28].

6.2 Outlook

Low-energy ion irradiation has a large potential to be utilized in modern nanoelectronics for implanting dopants like nitrogen into graphene. This work has shown the general feasibility of this approach, however, some obstacles still need to be overcome. Plasma treatments generally tend to have different effects even when the operating parameters are kept constant. There may be other properties that define the plasma more consistently than chamber pressure and acceleration and extraction voltage. If there was progress in the field of plasma reproducibility, it would certainly benefit the use of plasma treatments for the implantation of dopants into 2D materials. In the conducted experiments, the behavior of the plasma source could not be estimated well. Hence the use of a different plasma source may be rewarding. It is also thinkable that the implantation of nitrogen is possible without the requirement of additional heating as it was necessary in this setup. Furthermore, the application of this kind of plasma on different samples and materials can be tested. This includes specimens with multilayered graphene, graphene that was not CVD-synthesized, thicker carbon foils to minimize heating damages and materials like zinc selenide or telluride. The effects of different particle energies, ion dose rates and irradiation times concerning higher doping concentrations and the distribution of nitrogen species may be of interest as well. Regarding sample analysis, in situ irradiation in the microscope column and, as many observations during the experiments do not allow statistically confident deductions, the utilization of other forms of spectroscopy and microscopy, e.g. XPS for larger statistics regarding doping density and distribution of nitrogen species, should be considered. However, in order to reach reliable conclusions, efficient production of clean nitrogen-doped graphene samples is fundamental.

Appendix

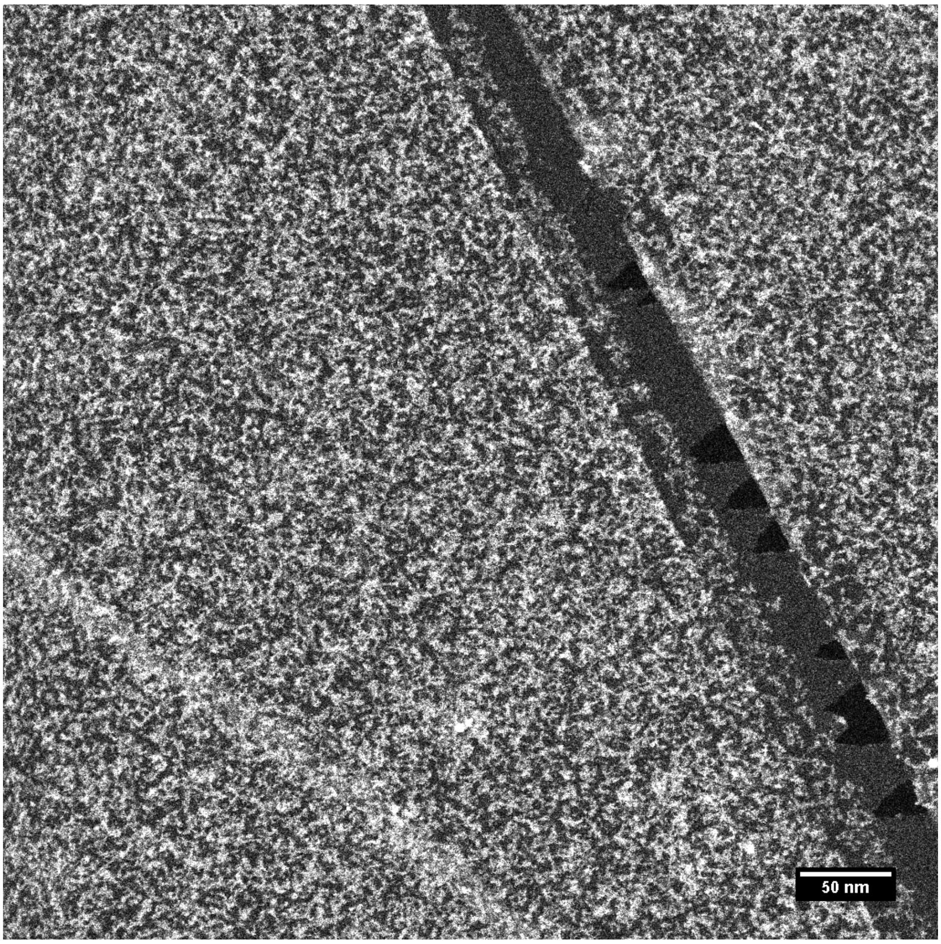

Figure A1: MAADF overview image of clean spot with FOV = 512 nm

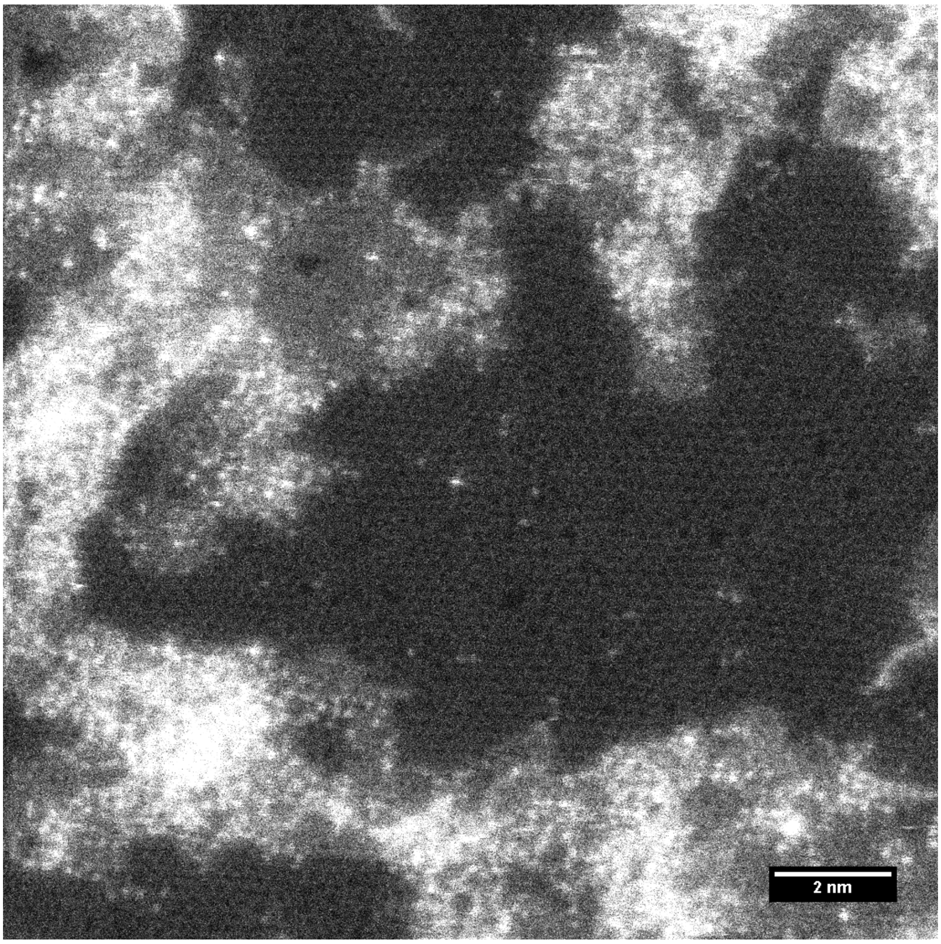

Figure A2: MAADF overview image at clean spot with FOV = 16 nm

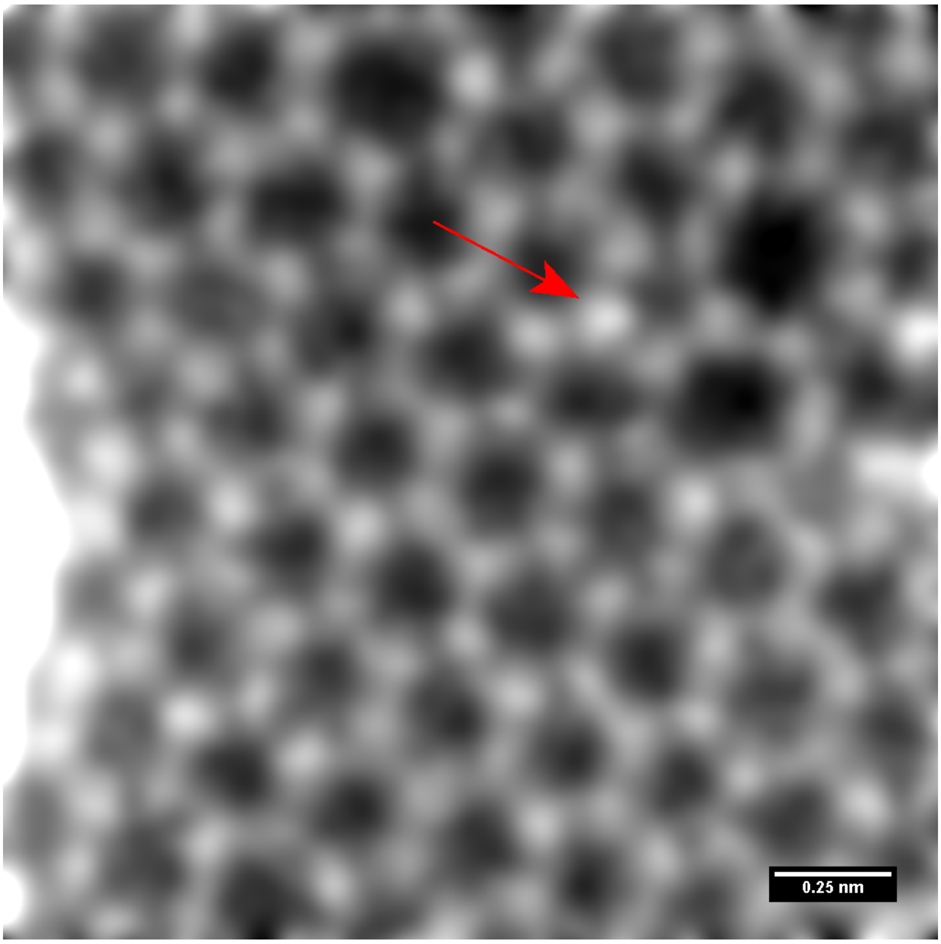

Figure A3: Full HAADF image corresponding to Figure 5.2

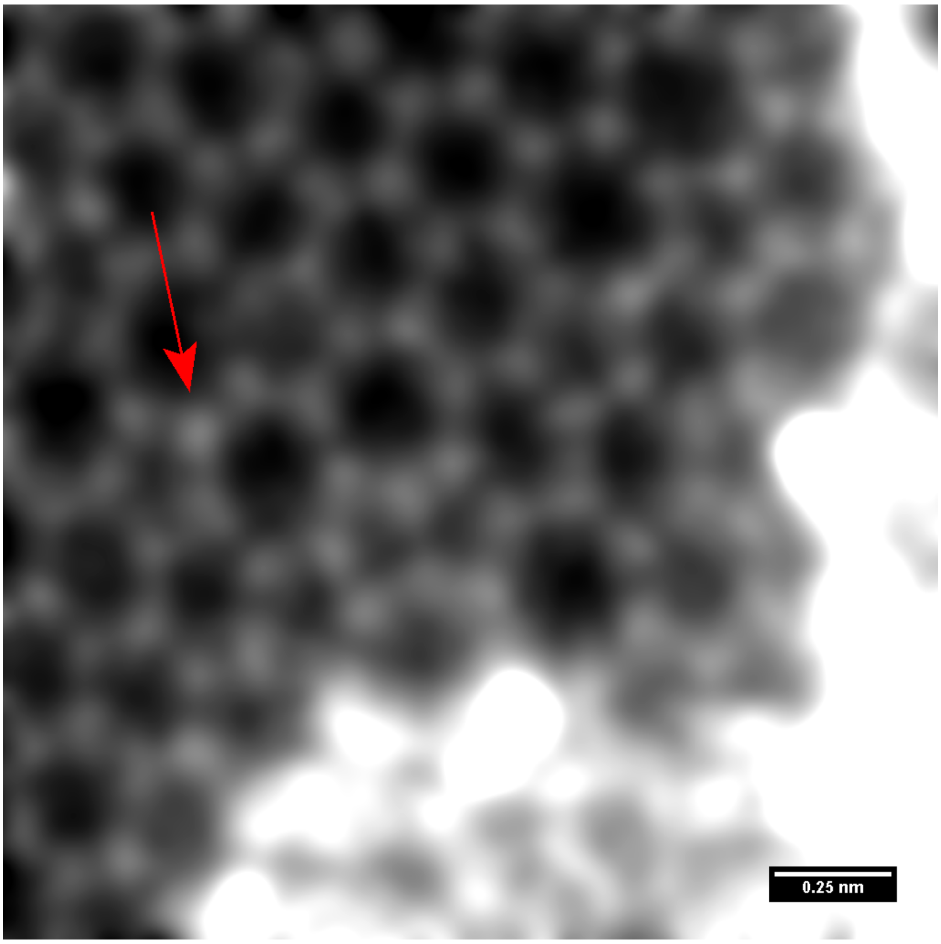

Figure A4: Full HAADF image corresponding to Figure 5.3

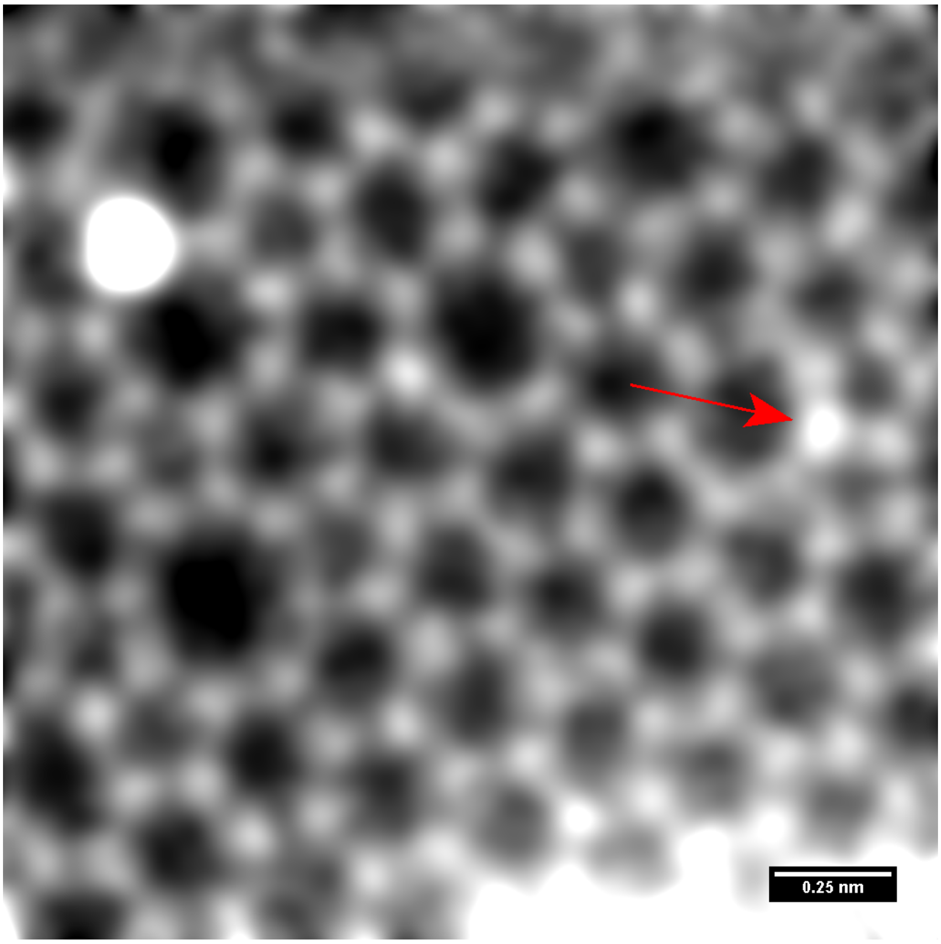

Figure A5: Full HAADF image corresponding to Figure 5.4a and b

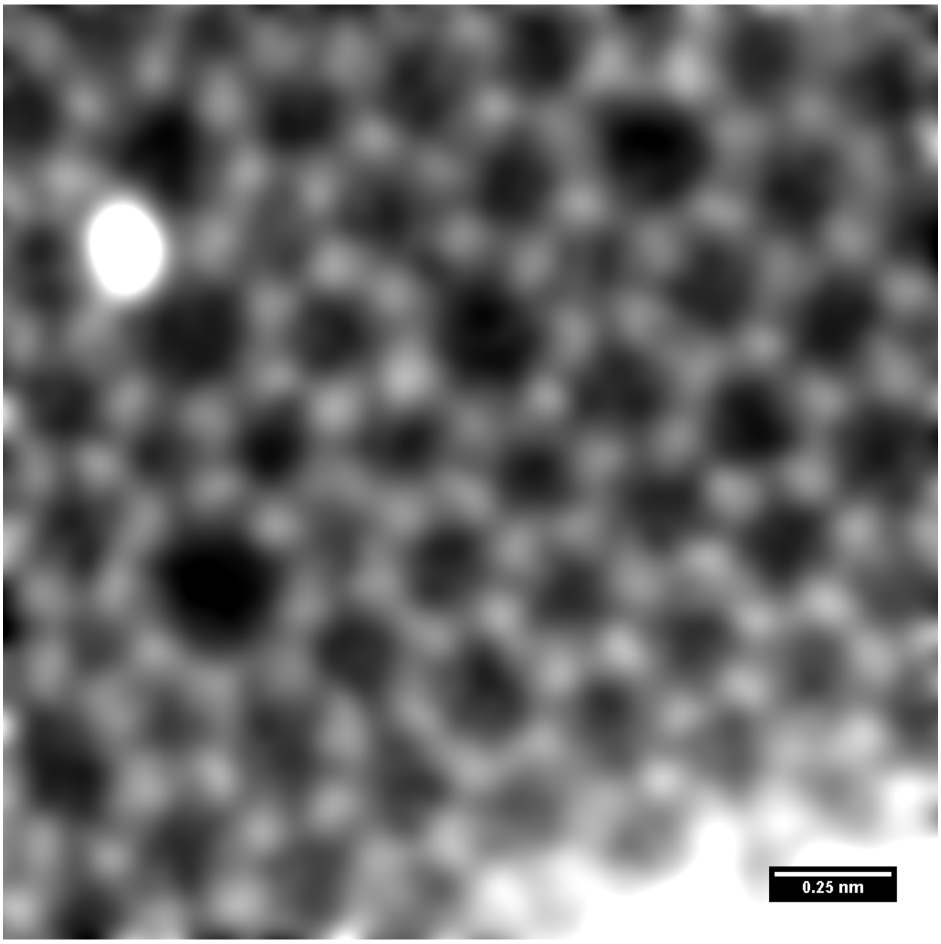

Figure A6: Full HAADF image corresponding to Figure 5.4c and d

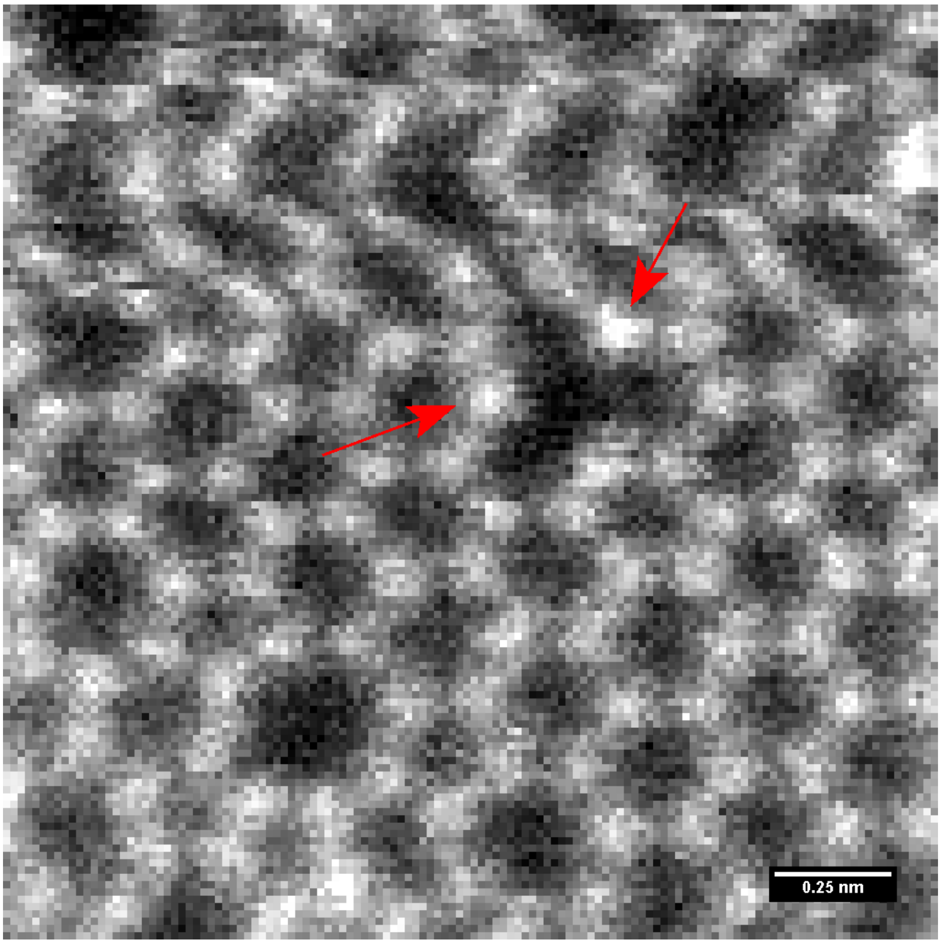

Figure A7: Full HAADF image corresponding to Figure 5.5

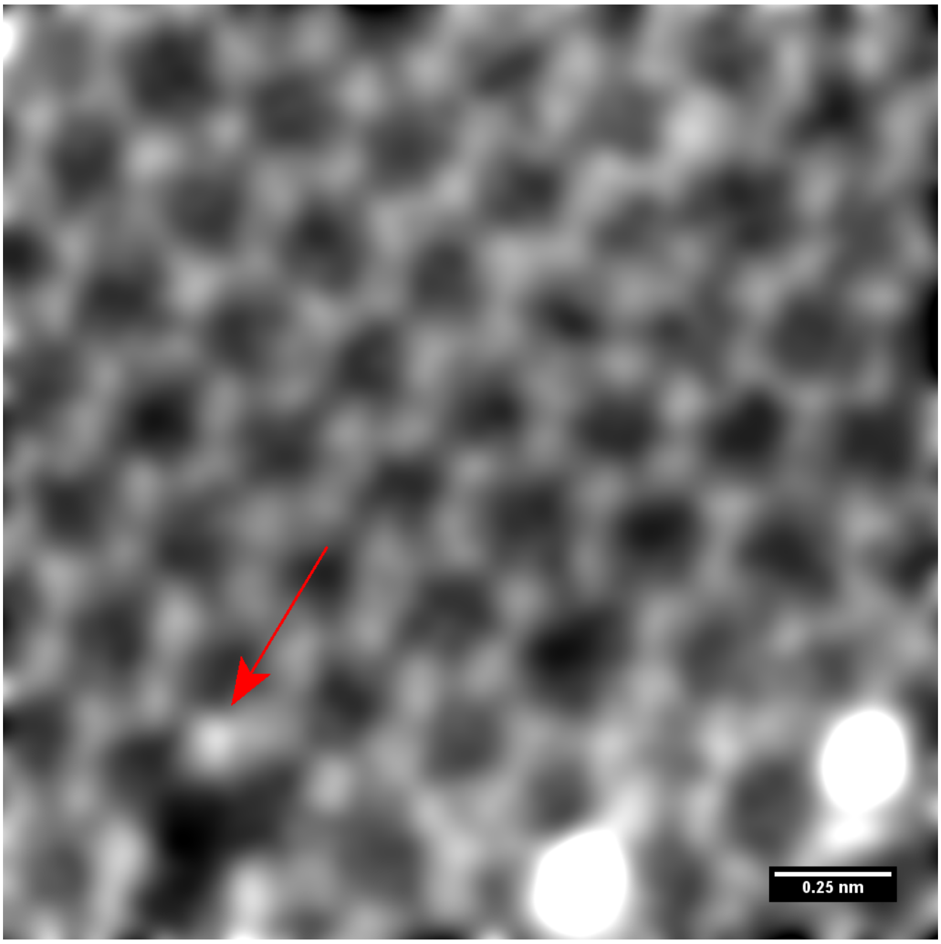

Figure A8: Full HAADF image corresponding to Figure 5.6a and b

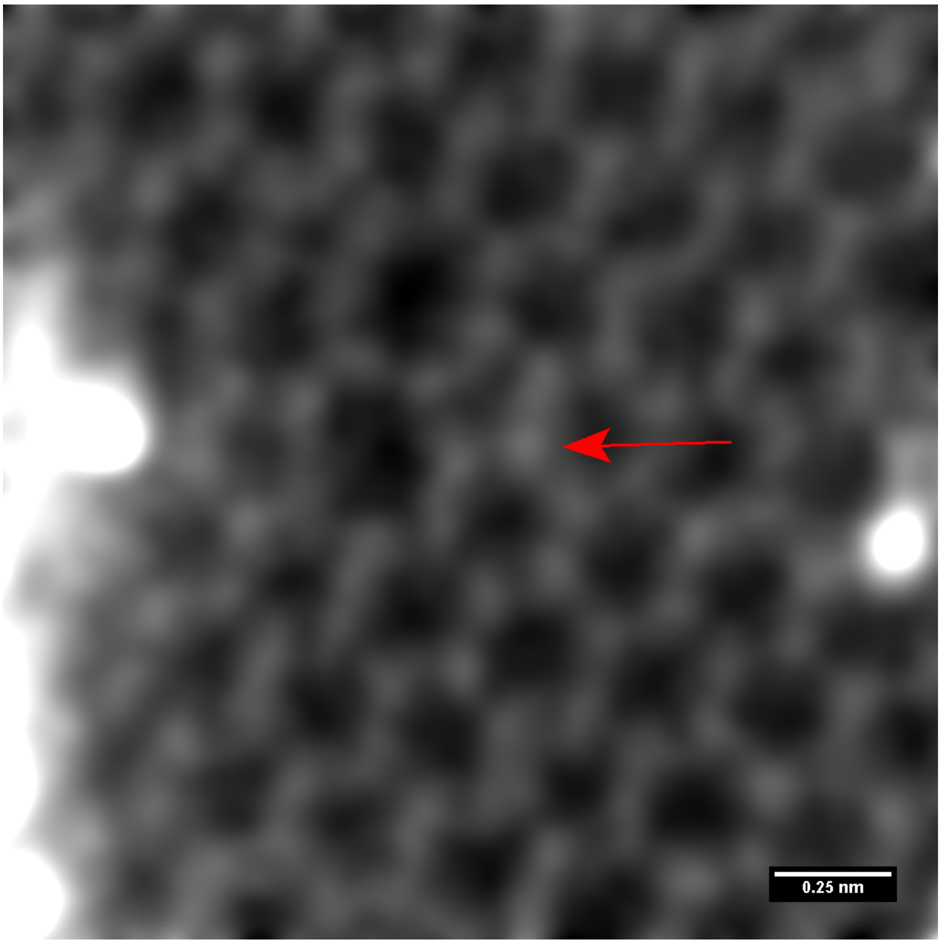

Figure A9: Full HAADF image corresponding to Figure 5.6c and d

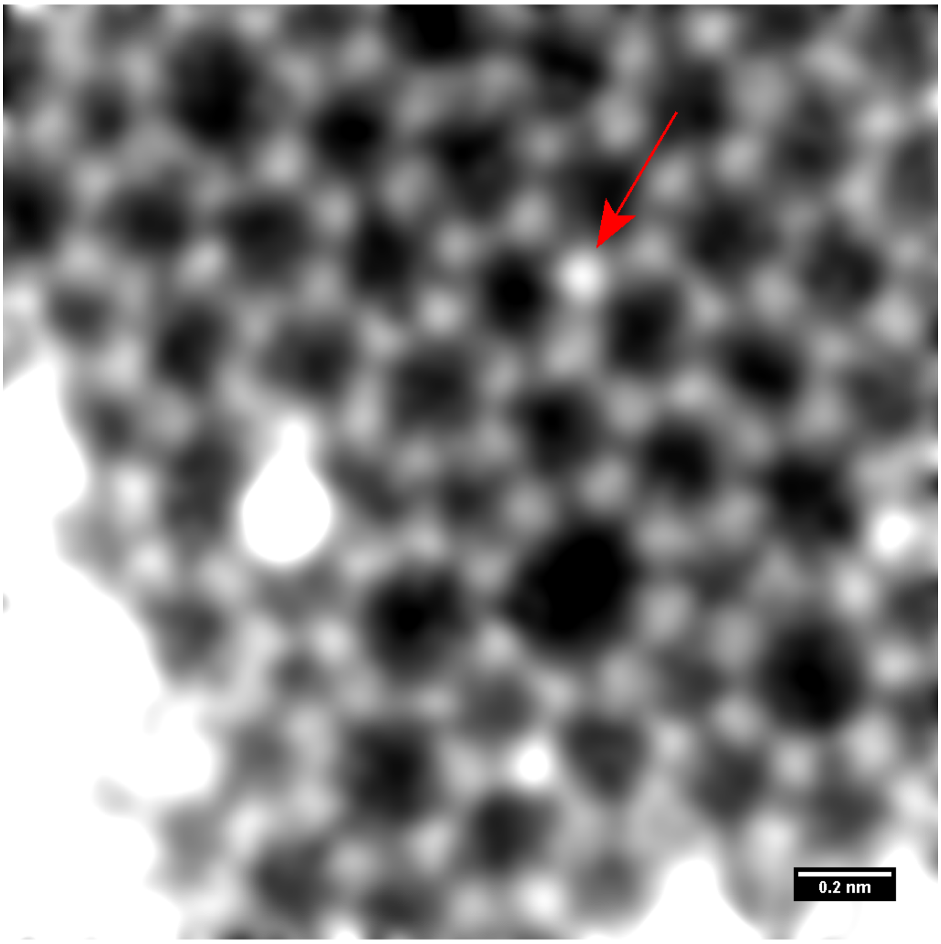

Figure A10: Full HAADF image corresponding to Figure 5.7

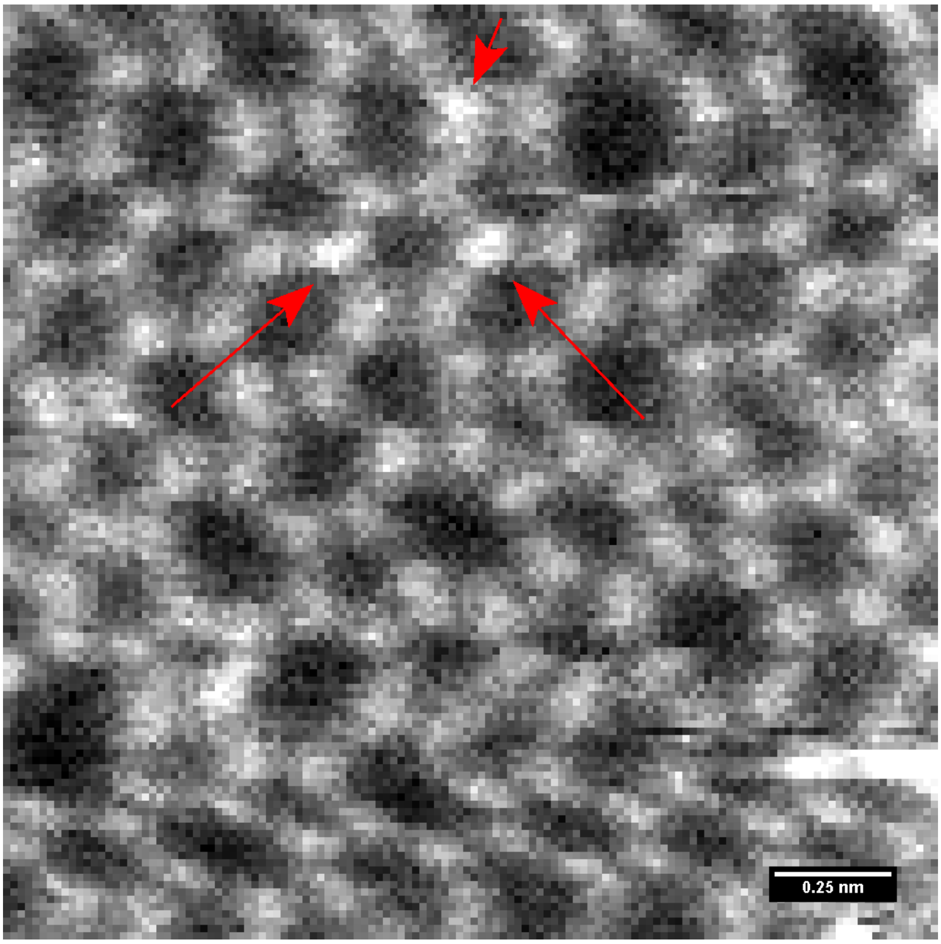

Figure A11: Full HAADF image corresponding to Figure 5.8

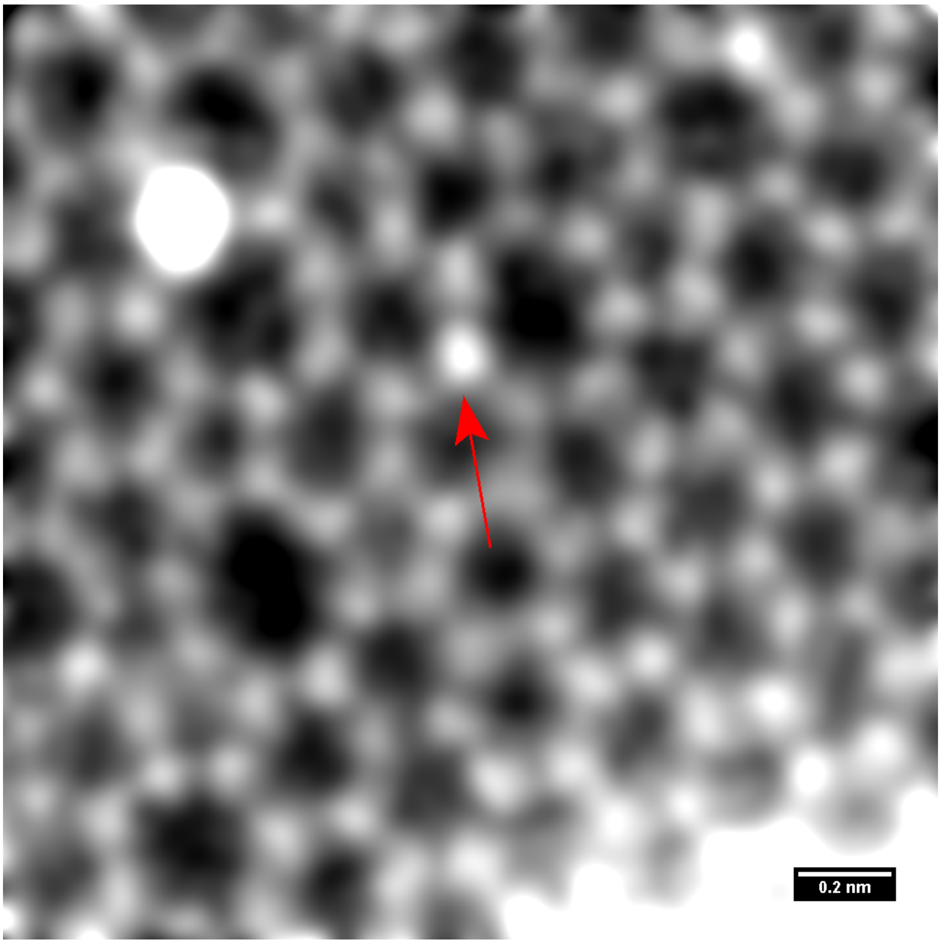

Figure A12: Full HAADF image corresponding to Figure 5.9a and b

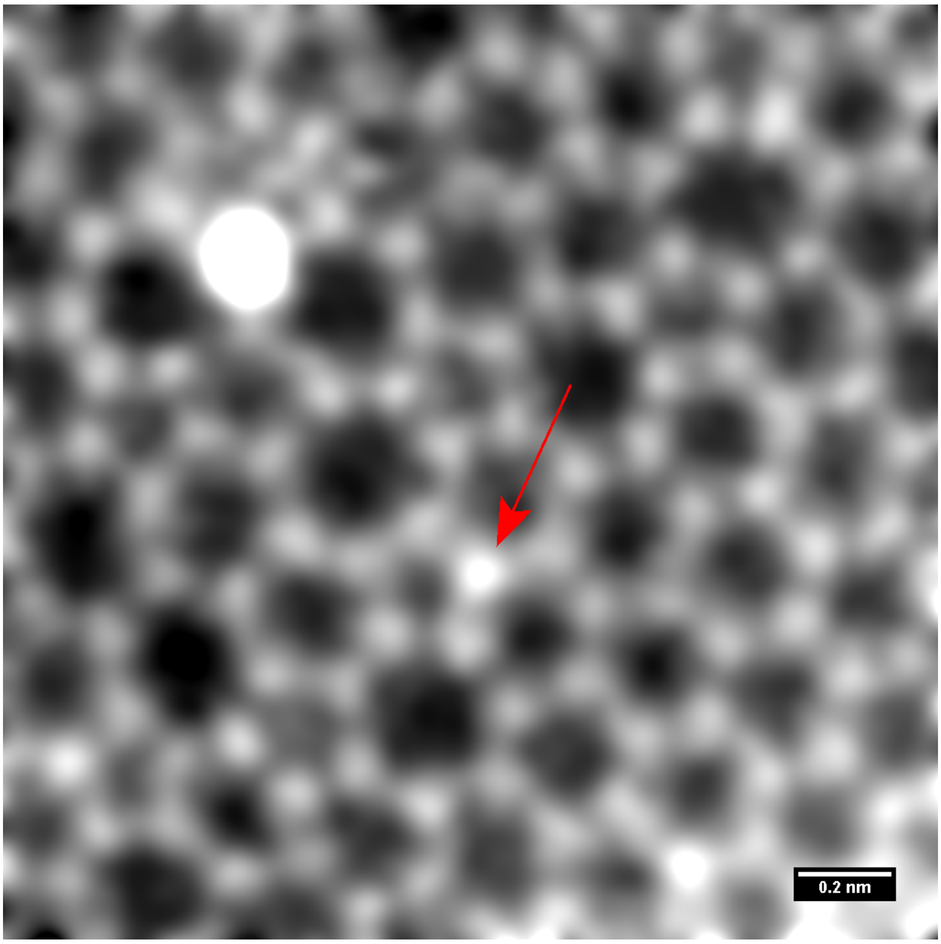

Figure A13: Full HAADF image corresponding to Figure 5.9c and d

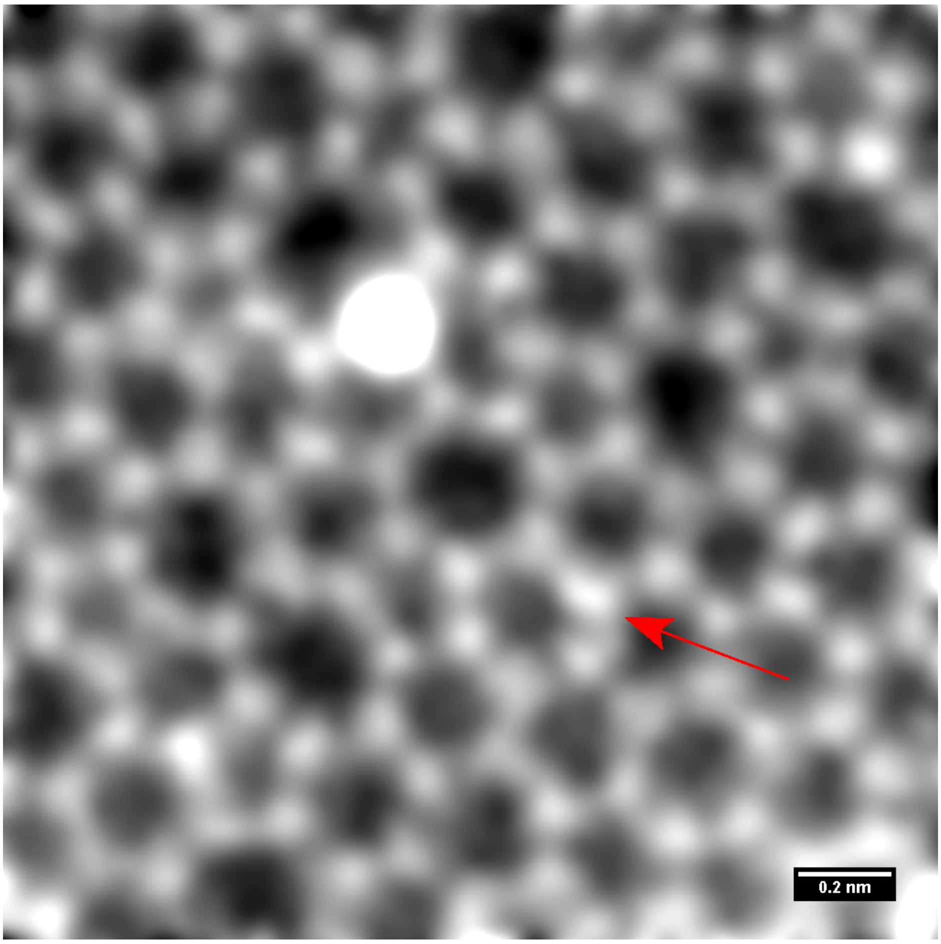

Figure A14: Full HAADF image corresponding to Figure 5.9e and f

List of Abbreviations

ADF	Annular Dark-Field
BF	Bright-Field
CCD	Charge-Coupled Device
CEOS	Corrected Electron Optical System (Company)
CFEG	Cold Field Emission Gun
CL	Condenser Lens
CVD	Chemical Vapor Deposition
DF	Dark-Field
DQE	Detection Quantum Efficiency
DV	Double Vacancy
ECR	Electron Cyclotron Resonance
EEL	Electron Energy Loss
EELS	Electron Energy Loss Spectroscopy
EM	Electron Microscopy/Microscope
FEG	Field-Emission Gun
FET	Field-Effect Transistor
FOV	Field of View
HAADF	High Angle Annular Dark Field
hBN	Hexagonal Boron-Nitride
HT	High Tension
MAADF	Medium Angle Annular Dark Field
MoS2	Molybdenum Disulfide
OL	Objective Lens
PC	Personal Computer
PL	Projector Lens
PM	Photomultiplier
QLM	Quadrupole Lens Module
SEM	Scanning Electron Microscopy
SLG	Single Layer Graphene
SNR	Signal-to-Noise-Ratio

STEM	Scanning Transmission Electron Microscopy/Microscope
STM	Scanning Tunneling Microscopy
SV	Single Vacancy
TEM	Transmission Electron Microscopy/Microscope
UHV	Ultra-High Vacuum
XPS	X-ray Photoelectron Spectroscopy

List of Nomenclature

α_{irr}	Largest irradiation half-angle, °
ΔE	Energy loss, eV
η	Cracking efficiency, %
A_C	Area per C atom in pristine graphene, nm^2
$A_{Faraday}$	Faraday cup surface area, mm^2
A_{flange}	Flange area, cm^2
a_{flange}	Distance from plasma source aperture to flange, cm
A_{FOV}	Field of view, nm^2
A_{irr}	Irradiated area, nm^2
a_{sample}	Distance from plasma source aperture to sample, cm
C_c	Chromatic aberration coefficient, mm
C_s	Spherical aberration coefficient, mm
d_{ap}	Aperture diameter, mm
e	Elementary charge, A s
$I_{Faraday}$	Ion current on Faraday cup, nA
I_{flange}	Ion current on flange, µA
I_{magn}	Magnetron current, mA
N	Ion dose, nm^{-2}
n	Ion dose rate, $\mathrm{nm}^{-2}\,\mathrm{min}^{-1}$
N_A	Avogadro constant, mol^{-1}
N_N	Amount of nitrogen atoms
$N_{doping,\%}$	Sample doping density, at.%

N_{doping}	Sample doping density, nm^{-2}
N_{flange}	Average ion dose on flange, nm^{-2}
n_{flange}	Average ion dose rate on flange, $\mathrm{nm}^{-2}\,\mathrm{min}^{-1}$
n_{gas}	Gas particle flow rate per sample area, $\mathrm{nm}^{-2}\,\mathrm{min}^{-1}$
N_{sample}	Average ion dose on sample, nm^{-2}
p_{ch}	Plasma chamber pressure, mbar
$P_{cleaning}$	Laser power during cleaning step, W
p_{gas}	Gas line pressure, mbar
P_{laser}	Laser power during irradiation step, W
p_t	Target chamber pressure, mbar
$R_{Fluke87}$	Internal resistance of Fluke 87, MΩ
r_{irr}	Radius of irradiated area, mm
T	Temperature, K
$t_{cleaning}$	Duration of laser cleaning step, s
t_{irr}	Irradiation time, min
U_{an}	Anode voltage, kV
U_{extr}	Extractor voltage, kV
$U_{Faraday}$	Faraday cup voltage, mV
V_M	Volume per mol, $\mathrm{L\,mol}^{-1}$
v_{pump}	Vacuum pump power, $\mathrm{L\,s}^{-1}$
Z	Atomic number

List of Figures

1.1 Structures related to graphene (top). Fullerene (bottom left), carbon nanotube (bottom center) and graphite (bottom right). It is illustrated how graphene could be wrapped up into fullerenes, rolled into nanotubes and stacked into graphite [4]. 2
1.2 Band structure of pristine Graphene based on nearest-neighbor tight-binding approximation [3] 3

2.1 Image of a fine FEG tungsten tip [24] 6
2.2 Systematic setup of a magnetic lens [24] 8
2.3 Illustration of electron-sample interactions with a thin specimen, self-created according to [24] 9

3.1 Nitrogen doping species in graphene, N1 showing pyridinic N, N2 pyrrolic N, N3 graphitic N and N4 graphitic "valley" N [27] 13
3.2 Dependency of perfect substitution probability on particle energy of nitrogen ions (blue) in graphene [13] 14
3.3 Probability of creation of pyridine-like N (blue) defect through introduction of a DV and subsequent capture of ion with respect to its original energy [13] 15
3.4 XPS-spectra including relative occurrences (left) and concentration (right) of N-species after different treatment steps [27], area under peaks is proportional to occurrence (left), N1-4 according to Figure 3.1, N1 pyridinic, N2 pyrrolic, N3 and N4 graphitic 17
3.5 (a) Double Gaussian filtered atomic resolution HAADF image of graphitic N, (b) raw HAADF image of area marked in a, (c) corresponding spectrum image in energy window 400-420 eV, (d) sum of EEL spectra from pixels around N atom [35] 18
3.6 One graphitic and five pyridinic N doping sites and their corresponding atomic models [28] 19

4.1 (a) Photo and (b) model of Nion UltraSTEM 100 [42] 32

5.1 Representative MAADF image at clean spot 36
5.2 Pyrrolic nitrogen doping site 1 37

5.3 Pyrrolic nitrogen doping site 2 37
5.4 Pyrrolic nitrogen doping site 3 38
5.5 Pyridinic nitrogen doping site 1 39
5.6 Pyridinic nitrogen doping site 2 40
5.7 Graphitic nitrogen doping site 1 41
5.8 Graphitic nitrogen doping site 2 42
5.9 Graphitic nitrogen doping site 3 43
5.10 Distribution of Nitrogen Species 46
5.11 Large area spectrum image 48

A1 MAADF overview image of clean spot with FOV = 512 nm 55
A2 MAADF overview image at clean spot with FOV = 16 nm 56
A3 Full HAADF image corresponding to Figure 5.2 57
A4 Full HAADF image corresponding to Figure 5.3 58
A5 Full HAADF image corresponding to Figure 5.4a and b 59
A6 Full HAADF image corresponding to Figure 5.4c and d 60
A7 Full HAADF image corresponding to Figure 5.5 61
A8 Full HAADF image corresponding to Figure 5.6a and b 62
A9 Full HAADF image corresponding to Figure 5.6c and d 63
A10 Full HAADF image corresponding to Figure 5.7 64
A11 Full HAADF image corresponding to Figure 5.8 65
A12 Full HAADF image corresponding to Figure 5.9a and b 66
A13 Full HAADF image corresponding to Figure 5.9c and d 67
A14 Full HAADF image corresponding to Figure 5.9e and f 68

List of Tables

4.1 Variables in Flange Ion Dose Calculation 24
4.2 Given and Measured Values for Flange Ion Dose Calculation 25
4.3 Additional Setup Parameters (Flange) 26
4.4 Variables in Gas Flow Ion Dose Calculation 26
4.5 Given and Measured Values for Gas Flow Ion Dose Calculation 27
4.6 Additional Setup Parameters (Gas Flow) 28
4.7 Variables in Faraday Cup Ion Dose Calculation 29
4.8 Given and Measured Values for Faraday Cup Ion Dose Calculation 29
4.9 Additional Setup Parameters (Faraday Cup) 29
4.10 Sample preparation procedure 31

5.1 Distribution of nitrogen species 45
5.2 Species and Structures of Nitrogen Atoms in Figure 5.11 50

Bibliography

[1] M. J. Allen, V. C. Tung, R. B. Kaner, *et al.*, “Honeycomb carbon: a review of graphene,” *Chemical reviews*, vol. 110, no. 1, p. 132, 2010.

[2] K. S. Novoselov, A. K. Geim, S. V. Morozov, D. Jiang, Y. Zhang, S. V. Dubonos, I. V. Grigorieva, and A. A. Firsov, “Electric field effect in atomically thin carbon films,” *science*, vol. 306, no. 5696, pp. 666–669, 2004.

[3] M. I. Katsnelson, “Graphene: carbon in two dimensions,” *Materials today*, vol. 10, no. 1, pp. 20–27, 2007.

[4] A. K. Geim and K. S. Novoselov, “The rise of graphene,” *Nature materials*, vol. 6, no. 3, pp. 183–191, 2007.

[5] A. C. Neto, F. Guinea, N. M. Peres, K. S. Novoselov, and A. K. Geim, “The electronic properties of graphene,” *Reviews of modern physics*, vol. 81, no. 1, p. 109, 2009.

[6] J. Meyer, A. Geim, M. Katsnelson, K. Novoselov, D. Obergfell, S. Roth, C. Girit, and A. Zettl, “On the roughness of single-and bi-layer graphene membranes,” *Solid State Communications*, vol. 143, no. 1, pp. 101–109, 2007.

[7] C. Lee, X. Wei, J. W. Kysar, and J. Hone, “Measurement of the elastic properties and intrinsic strength of monolayer graphene,” *science*, vol. 321, no. 5887, pp. 385–388, 2008.

[8] A. A. Balandin, S. Ghosh, W. Bao, I. Calizo, D. Teweldebrhan, F. Miao, and C. N. Lau, “Superior thermal conductivity of single-layer graphene,” *Nano letters*, vol. 8, no. 3, pp. 902–907, 2008.

[9] Y. Zhang, L. Zhang, and C. Zhou, “Review of chemical vapor deposition of graphene and related applications,” *Accounts of chemical research*, vol. 46, no. 10, pp. 2329–2339, 2013.

[10] P. Avouris and F. Xia, “Graphene applications in electronics and photonics,” *Mrs Bulletin*, vol. 37, no. 12, pp. 1225–1234, 2012.

[11] K. M. Shahil and A. A. Balandin, “Thermal properties of graphene and multilayer graphene: Applications in thermal interface materials,” *Solid State Communications*, vol. 152, no. 15, pp. 1331–1340, 2012.

[12] X. Li, X. Wang, L. Zhang, S. Lee, and H. Dai, “Chemically derived, ultrasmooth graphene nanoribbon semiconductors,” *science*, vol. 319, no. 5867, pp. 1229–1232, 2008.

[13] E. Åhlgren, J. Kotakoski, and A. Krasheninnikov, “Atomistic simulations of the implantation of low-energy boron and nitrogen ions into graphene,” *Physical Review B*, vol. 83, no. 11, p. 115424, 2011.

[14] D. Usachov, O. Vilkov, A. Gruneis, D. Haberer, A. Fedorov, V. Adamchuk, A. Preobrajenski, P. Dudin, A. Barinov, M. Oehzelt, *et al.*, “Nitrogen-doped graphene: efficient growth, structure, and electronic properties,” *Nano letters*, vol. 11, no. 12, pp. 5401–5407, 2011.

[15] M. Taghioskoui, “Trends in graphene research,” *Materials today*, vol. 12, no. 10, pp. 34–37, 2009.

[16] H. Wang, T. Maiyalagan, and X. Wang, “Review on recent progress in nitrogen-doped graphene: synthesis, characterization, and its potential applications,” *Acs Catalysis*, vol. 2, no. 5, pp. 781–794, 2012.

[17] A. L. M. Reddy, A. Srivastava, S. R. Gowda, H. Gullapalli, M. Dubey, and P. M. Ajayan, “Synthesis of nitrogen-doped graphene films for lithium battery application,” *ACS nano*, vol. 4, no. 11, pp. 6337–6342, 2010.

[18] D. Pan, S. Wang, B. Zhao, M. Wu, H. Zhang, Y. Wang, and Z. Jiao, “Li storage properties of disordered graphene nanosheets,” *Chemistry of Materials*, vol. 21, no. 14, pp. 3136–3142, 2009.

[19] L. Qu, Y. Liu, J.-B. Baek, and L. Dai, “Nitrogen-doped graphene as efficient metal-free electrocatalyst for oxygen reduction in fuel cells,” *ACS nano*, vol. 4, no. 3, pp. 1321–1326, 2010.

[20] S. Yang, X. Feng, X. Wang, and K. Müllen, “Graphene-based carbon nitride nanosheets as efficient metal-free electrocatalysts for oxygen reduction reactions,” *Angewandte Chemie International Edition*, vol. 50, no. 23, pp. 5339–5343, 2011.

[21] H. M. Jeong, J. W. Lee, W. H. Shin, Y. J. Choi, H. J. Shin, J. K. Kang, and J. W. Choi, “Nitrogen-doped graphene for high-performance ultracapacitors and the importance of nitrogen-doped sites at basal planes,” *Nano letters*, vol. 11, no. 6, pp. 2472–2477, 2011.

[22] Y. Wang, Y. Shao, D. W. Matson, J. Li, and Y. Lin, “Nitrogen-doped graphene and its application in electrochemical biosensing,” *ACS nano*, vol. 4, no. 4, pp. 1790–1798, 2010.

[23] R. F. Egerton, *Physical principles of electron microscopy.* Springer, 2005.

[24] D. B. Williams and C. B. Carter, “The transmission electron microscope,” in *Transmission electron microscopy*, pp. 3–17, Springer, 1996.

[25] B. Fultz and J. M. Howe, *Transmission electron microscopy and diffractometry of materials*. Springer Science & Business Media, 2012.

[26] O. Scherzer, “Über einige Fehler von Elektronenlinsen,” *Zeitschrift für Physik*, vol. 101, no. 9-10, pp. 593–603, 1936.

[27] M. Scardamaglia, B. Aleman, M. Amati, C. Ewels, P. Pochet, N. Reckinger, J.-F. Colomer, T. Skaltsas, N. Tagmatarchis, R. Snyders, *et al.*, “Nitrogen implantation of suspended graphene flakes: annealing effects and selectivity of sp 2 nitrogen species,” *Carbon*, vol. 73, pp. 371–381, 2014.

[28] Y.-C. Lin, P.-Y. Teng, C.-H. Yeh, M. Koshino, P.-W. Chiu, and K. Suenaga, “Structural and chemical dynamics of pyridinic-nitrogen defects in graphene,” *Nano letters*, vol. 15, no. 11, pp. 7408–7413, 2015.

[29] M. Telychko, P. Mutombo, M. Ondracek, P. Hapala, F. C. Bocquet, J. Kolorenc, M. Vondracek, P. Jelinek, and M. Svec, “Achieving high-quality single-atom nitrogen doping of graphene/sic (0001) by ion implantation and subsequent thermal stabilization,” *ACS nano*, vol. 8, no. 7, pp. 7318–7324, 2014.

[30] B. Guo, Q. Liu, E. Chen, H. Zhu, L. Fang, and J. R. Gong, “Controllable n-doping of graphene,” *Nano letters*, vol. 10, no. 12, pp. 4975–4980, 2010.

[31] Y.-P. Lin, Y. Ksari, D. Aubel, S. Hajjar-Garreau, G. Borvon, Y. Spiegel, L. Roux, L. Simon, and J.-M. Themlin, “Efficient and low-damage nitrogen doping of graphene via plasma-based methods,” *Carbon*, vol. 100, pp. 337–344, 2016.

[32] W. Zhao, O. Hofert, K. Gotterbarm, J. Zhu, C. Papp, and H.-P. Steinruck, “Production of nitrogen-doped graphene by low-energy nitrogen implantation,” *The Journal of Physical Chemistry C*, vol. 116, no. 8, pp. 5062–5066, 2012.

[33] S. H. Park, J. Chae, M.-H. Cho, J. H. Kim, K.-H. Yoo, S. W. Cho, T. G. Kim, and J. W. Kim, “High concentration of nitrogen doped into graphene using n 2 plasma with an aluminum oxide buffer layer,” *Journal of Materials Chemistry C*, vol. 2, no. 5, pp. 933–939, 2014.

[34] M. Rybin, A. Pereyaslavtsev, T. Vasilieva, V. Myasnikov, I. Sokolov, A. Pavlova, E. Obraztsova, A. Khomich, V. Ralchenko, and E. Obraztsova, “Efficient nitrogen doping of graphene by plasma treatment,” *Carbon*, vol. 96, pp. 196–202, 2016.

[35] U. Bangert, W. Pierce, D. Kepaptsoglou, Q. Ramasse, R. Zan, M. Gass, J. Van den Berg, C. Boothroyd, J. Amani, and H. Hofsass, “Ion implantation of graphene toward ic compatible technologies,” *Nano letters*, vol. 13, no. 10, pp. 4902–4907, 2013.

[36] O. L. Krivanek, M. F. Chisholm, V. Nicolosi, T. J. Pennycook, G. J. Corbin, N. Dellby, M. F. Murfitt, C. S. Own, Z. S. Szilagyi, M. P. Oxley, *et al.*, “Atom-by-atom structural and chemical analysis by annular dark-field electron microscopy,” *Nature*, vol. 464, no. 7288, pp. 571–574, 2010.

[37] D. Wei, Y. Liu, Y. Wang, H. Zhang, L. Huang, and G. Yu, "Synthesis of n-doped graphene by chemical vapor deposition and its electrical properties," *Nano letters*, vol. 9, no. 5, pp. 1752–1758, 2009.

[38] Z. Luo, S. Lim, Z. Tian, J. Shang, L. Lai, B. MacDonald, C. Fu, Z. Shen, T. Yu, and J. Lin, "Pyridinic n doped graphene: synthesis, electronic structure, and electrocatalytic property," *Journal of Materials Chemistry*, vol. 21, no. 22, pp. 8038–8044, 2011.

[39] Y. Fujimoto and S. Saito, "Formation, stabilities, and electronic properties of nitrogen defects in graphene," *Physical Review B*, vol. 84, no. 24, p. 245446, 2011.

[40] T. Susi, J. Kotakoski, R. Arenal, S. Kurasch, H. Jiang, V. Skakalova, O. Stephan, A. V. Krasheninnikov, E. I. Kauppinen, U. Kaiser, *et al.*, "Atomistic description of electron beam damage in nitrogen-doped graphene and single-walled carbon nanotubes," *ACS nano*, vol. 6, no. 10, pp. 8837–8846, 2012.

[41] J. C. Meyer, F. Eder, S. Kurasch, V. Skakalova, J. Kotakoski, H. J. Park, S. Roth, A. Chuvilin, S. Eyhusen, G. Benner, *et al.*, "Accurate measurement of electron beam induced displacement cross sections for single-layer graphene," *Physical review letters*, vol. 108, no. 19, p. 196102, 2012.

[42] O. Krivanek, G. Corbin, N. Dellby, B. Elston, R. Keyse, M. Murfitt, C. Own, Z. Szilagyi, and J. Woodruff, "An electron microscope for the aberration-corrected era," *Ultramicroscopy*, vol. 108, no. 3, pp. 179–195, 2008.

[43] C. Ewels and M. Glerup, "Nitrogen doping in carbon nanotubes," *Journal of nanoscience and nanotechnology*, vol. 5, no. 9, pp. 1345–1363, 2005.